Postprint of: Kowalkińska M., Dudziak S., Karczewski J., Ryl J., Trykowski G., Zielińska-Jurek A., Facet effect of TiO_2 nanostructures from $TiOF_2$ and their photocatalytic activity, CHEMICAL ENGINEERING JOURNAL, Vol. 404, (2021), 126493, DOI: 10.1016/j.cej.2020.126493

Facet effect of TiO_2 nanostructures from $TiOF_2$ and their photocatalytic activity

Marta Kowalkińska[1], Szymon Dudziak[1], Jakub Karczewski[2], Jacek Ryl[3], Grzegorz Trykowski[4], Anna Zielińska-Jurek[1*]

[1] Department of Process Engineering and Chemical Technology, Faculty of Chemistry, Gdansk University of Technology (GUT), G. Narutowicza 11/12, 80-233 Gdansk, Poland

[2] Department of Solid State Physics, Faculty of Applied Physics and Mathematics, Gdansk University of Technology (GUT), 80-233 Gdansk, Poland

[3] Department of Electrochemistry, Corrosion and Materials Engineering, Gdansk University of Technology (GUT), 80-233 Gdansk, Poland

[4]Faculty of Chemistry, Nicolaus Copernicus University, Gagarina 7, 87-100 Toruń, Poland

* Corresponding author: annjurek@pg.edu.pl

Abstract

In this study, special attention is focused on the design of TiO_2 morphology and microstructure in the two-step preparation procedure using $TiOF_2$ as a precursor to study their photodegradation mineralization efficiency. Firstly, $TiOF_2$ was synthesized by a simple solvothermal method using titanium(IV) tetrafluoride, which was further used as a precursor in preparation of anatase 2D nanosheets, octahedral, decahedral, and rectangular prisms shape structures. The as-obtained nanostructures were characterized by X-ray diffraction (XRD), scanning electron microscopy (SEM), Brunauer-Emmett-Teller surface area analysis (BET), X-ray photoelectron spectroscopy (XPS), UV-vis diffuse reflectance spectroscopy and photoluminescence spectroscopy. It was assumed that $TiOF_2$ could be applied as a useful precursor for the preparation of nanostructured TiO_2 with defined morphology. Simple controlling of the reaction environment, together with the stabilizing effect of the introduced substrates, resulted in the formation of TiO_2 particles with different morphologies and

consequently exposed crystal facets. The presence of {001}, {101} and {100} facets influence on their photocatalytic activity but mostly on their mineralization efficiency and the pathway of phenol degradation. From the obtained series, the TiO_2 octahedra exposing {101} facets exhibited the highest photoactivity and mineralization efficiency under UV-Vis light irradiation, which decreases as the other facets appear and become more exposed. The obtained results were compared with a computational study on the ·OH and $\cdot O_2^-$ attack on the phenyl ring. Overall results showed that the surface effects of the photocatalyst could be an influencing factor in both mineralization efficiency and photodegradation products formation.

Keywords: titanium oxyfluoride, TiO_2 surface structure, TOC mineralization, phenol degradation

1. Introduction

Through the last years, titanium(IV) oxide has established itself as one of the most important wide-gap semiconducting material with numerous applications. Due to its excellent chemical stability, electron transport properties and overall availability it is being studied as a pure or modified material for sensors development [1], electronic devices [2], self-cleaning materials [3] and photoanodes preparation [4]. Moreover, it remains as one of the most important material that is continuously used in the field of photocatalysis. Although a great effort was made to understand and utilize TiO_2 properties as a photocatalyst, some questions and unknown details are still present, mostly regarding interactions between TiO_2 and reacting substrates. More recently, this has led to significant attention being given to preparation and studying activity of nanostructured TiO_2 particles, exposing specific crystal facets, to describe the photocatalytic process on its fundamental level [5–8]. Reported findings have shown that surface structure can remarkably influence on reactivity towards H_2 generation and storage [9-10], oxidation of organic compounds [11-12], generation of reactive radicals [13], CO_2 photoconversion to methane [14] and gas sensing ability of TiO_2 [15]. It can be controlled by growing TiO_2 particles

in a specific environment, from which HF, ammonium-bearing compounds (amines, hydrazine), alcohols and pH regulators were found to influence significantly on particles morphology [16–22]. However, it is still challenging to find a preparation method that would limit the chemicals required to control TiO_2 crystallization without compromising a variety of its possible structures.

In this regard, titanium-fluorine compounds can be seen as useful precursors, as they naturally introduce fluorine ions inside the reaction system. Moreover, compounds like $(NH_4)_2TiF_6$ or TiF_4 can be easily obtained from the processing of $Fe_2O_3 \cdot TiO_2$ minerals [23–25]. Within this group, TiF_4 was already introduced, with great success, as a substrate in the preparation of anatase decahedrons and platelets [16], however, their direct synthesis results in the formation of large, micro-sized particles, which is unfavourable for their application in photocatalysis. As an alternative approach, Gordon *et al.* have obtained series of TiO_2 nanostructures from TiF_4 by dissolving and subsequent crystal growing in mixtures of organic surfactants [6], which remain as a rather complex and waste-generating method. On the other hand, $(NH_4)_2TiF_6$ was used in a solid-state reaction, where final TiO_2 morphology results from coalescence of calcined particles, which were obtained only in the form of nanosheets [26].

However, an alternative way can be emerged from solvothermal processing of titanium oxyfluoride $TiOF_2$, utilizing fact of its easy degradation to TiO_2. Titanium oxyfluoride is a metastable phase which exists in two known polymorphs, the first one with cubic structure (space group Pm-3m) and the second with hexagonal (space group R-3c). Both of them are composed of titanium atoms octahedrally coordinated by randomly distributed oxygen and fluorine, which are then connected differently. The unit cells of both structures, visualized by the VESTA program, are presented in Figure 1. Usually, $TiOF_2$ with cubic structure is synthesized through partial hydrolysis/oxidation of titanium butoxide or TiF_4 [27–30]. However, it can also be obtained through the fluorination of TiO_2 [31]. Although pure $TiOF_2$

was found to be active under visible light [32-33], its possible photocatalytic activity under a broad spectrum is rather low, comparing to TiO_2 [34]. In this regard, it was applied as a precursor for the synthesis of TiO_2 or $TiO_2/TiOF_2$. At present, only (001) plane-exposing anatase was formed from $TiOF_2$, which is not always desired [11-12]. Therefore, in this study, the possibility to create a variety of TiO_2 structures, followed by their activity analysis, starting from $TiOF_2$ precursor and with the addition of possibly simple growth-controlling agents, was investigated. The effect of octahedral, decahedral, and rectangular prisms shape of TiO_2 on the ability to mineralize organic pollutants was further investigated. The correlation between anatase (001) and (101) surfaces ratio, and mineralization efficiency was studied in detail. Moreover, computationally analysis by calculating the minimum energy path (MEP) of radical addition at the *ortho* and *para* positions was applied to study the participation of ·OH and $\cdot O_2^-$ radicals in phenol molecule degradation. The initial and final structures were geometry optimized using DFT calculations with PBE0 hybrid functional and the D3BJ dispersion correction.

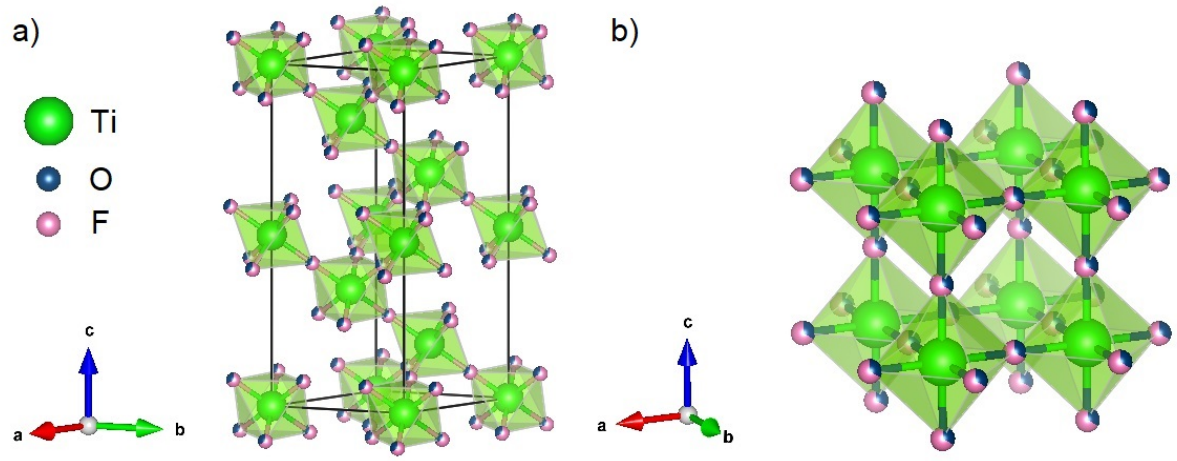

Figure 1. Visualization of a) hexagonal $TiOF_2$ unit cell, b) cubic $TiOF_2$ unit cell.

The probability of distribution in lattice is 1/3 for oxygen and 2/3 for fluorine

2. Experimental section

The synthesis of titanium oxyfluoride and titanium(IV) oxide nanostructures were proceeded by a facile solvothermal method. Titanium(IV) tetrafluoride, 1-butanol, hydrofluoric acid (48%), hydrochloric acid (35%), hydrazine hydrate (60%) and ammonia water (25%) were used as received from Sigma-Aldrich without any purification.

2.1. Fabrication of $TiOF_2$ precursor

In the preparation of $TiOF_2$ precursor, 10 g of TiF_4 powder was added into a 200 cm^3 Teflon reactor with 120 cm^3 of 1-butanol (without introducing any HF). Obtained mixture was stirred for 15 minutes to form stable suspension using a Teflon-coated magnetic stirrer bar. After that, the reactor was transferred into a stainless-steel autoclave immediately and was heated at 210°C for 24 h. The obtained product was separated through centrifugation and was washed thoroughly with absolute ethanol and deionized water to remove the residual contamination and fluorine species. After drying at 80°C, the $TiOF_2$ grey precursor was harvested.

2.2. The synthesis of TiO_2 nanostructures

In the second step, the obtained $TiOF_2$ precursor was hydrothermally treated to form nanostructured TiO_2. Different capping agents (hydrochloric acid, hydrofluoric acid, hydrazine, and ammonia) were selected as growth-controlling species, based on the previous reports [35-37]. In a typical synthesis, 0.25 g of as-synthesized $TiOF_2$ was dissolved in a 100 cm^3 mixture of deionized water and stabilizing agent and was transferred into a 200 cm^3 autoclave after 15 minutes of stirring. The prepared suspension was heated at 210°C for 24 h, then cooled down naturally. Obtained precipitates were centrifuged, washed, and dried the same way as during fabrication of the precursor, to obtain white powders of TiO_2. Moreover, TiO_2_H_2O sample was synthesized as previously described in 100 cm^3 of deionized water as a medium, without introducing any growth-controlling agent. Detailed information regarding the synthesis conditions of the obtained samples and their description is presented in Table 1.

To show the critical effect of the size change on the activity of the obtained photocatalyst the comparison of nanosheets prepared directly from TiF_4 to structures obtained from $TiOF_2$ was performed.

Table 1. Synthesis conditions of the obtained samples

Sample name	Precursor	Precursor amount [g]	Medium		Volume [cm^3]	
			Solvent	Capping agent	Solvent	Capping agent
$TiOF_2$	TiF_4	10	1-butanol	-	120	-
TiO_2_HCl	$TiOF_2$	0.25	water	HCl	98	2
TiO_2_HF/HCl				HF and HCl	99	0.25/0.75
TiO_2_HF				HF	99.75	0.25
TiO_2_H_2O				-	100	-
TiO_2_N_2H_4				$N_2H_4 \cdot H_2O$	75	25
TiO_2_NH_3				$NH_3 \cdot H_2O$	47	53

Briefly, anatase sheets were solvothermaly synthesised directly from TiF_4 in the presence of 1-butanol and with addition of hydrofluoric acid. For a synthesis a 3.06 g of TiF_4 was introduced to the 120 cm^3 of 1-butanol inside a 200 cm^3 Teflon lined reactor and 0.68 cm^3 of HF (48%) was subsequently added. Then, the mixture was transferred to an oven and was kept in 210°C for 24 h. Obtained TiO_2 particles were centrifuged, washed with water, dried at 80°C and finally calcined at 500°C to remove residual F^-.

2.3. Material characterization

The structure of the samples and phase composition were investigated by X-ray powder diffraction (Cu Kα radiation, Rigaku MiniFlex 600 X-Ray diffractometer). The analysis and Rietveld refinements were performed with the HighScorePlus software package (PANalytical, 2006) and the ICDD database with data fitting based on the pseudo-Voigt profile function. The specimen displacement, lattice parameters, polynomial coefficients for the background function, profile parameters, and Gaussian and Lorentzian profile coefficients were refined. The amorphous phase content was analyzed using an internal standard (NiO, Aldrich, Germany).

The morphologies of the nanostructures were characterized by field emission scanning electron microscope (SEM, FEI Quanta FEG 250). The selected area electron diffraction (SAED) analysis were performed using the transmission electron microscope (TEM) Tecnai 20F X-Twin, an electron source, cathode with field emission gun (FEG), EHT=200keV, camera for TEM Orius, Gatan Inc. The Brunauer-Emmett-Teller (BET) surface area of the powders was analysed by nitrogen adsorption using a Micromeritics Gemini V instrument. All samples were degassed at 200°C prior to nitrogen adsorption measurements. The BET surface area was determined by a multipoint BET method. The chemical states on the surface of nanostructures were determined by X-ray photoelectron spectroscopy (XPS) using Escalab 250Xi (Thermo Fisher Scientific, Waltham, USA) with Al Kα radiation and pass energy 20 eV. The optical properties were studied by a UV–Vis spectrophotometer (Thermo Fisher Scientific Evolution 220) for the measurement of diffuse reflectance (DRS), using $BaSO_4$ as a standard. Based on the obtained data, the bandgap energy calculations were performed using Tauc's method. The photoluminescence (PL) spectra were recorded on a Perkin-Elmer LS 55 spectrophotometer with a Xe discharge lamp as the excitation source. The samples were excited at 250 nm in the air at room temperature. During measurements, a 290 nm cut-off filter was used.

2.4. Determination of photocatalytic activity

Photocatalytic activity of obtained samples was tested in a model reaction of phenol degradation, performed in the black-box. All mentioned chemicals were used as delivered by the provider and were used without any purification.

In a typical experiment of phenol degradation, 25 cm^3 of pollutant solution (20 $mg \cdot dm^{-3}$, diluted from the concentrated stock solution) and 50 mg of photocatalyst were put into a 25 cm^3 quartz reactor under stirring. A Xe lamp (model 6271H, Oriel, USA) with a water IR filter, emitting light from the UV-Vis range, was used as a light source and the system was set up to obtain the measured UV-spectrum flux intensity at the reactor border equal to 30 $mW \cdot cm^{-2}$.

During the reaction, a constant air flow of 5 $dm^3 \cdot h^{-1}$ was introduced through suspension, which was magnetically stirred and thermostated at 20°C. Before irradiation, the whole system was kept in the dark for 30 minutes to achieve the adsorption-desorption equilibrium. After that, the process was initiated by turning on the Xe lamp. All the experiments were studied for 60 min of irradiation. Samples were collected at -30, -15, 0, 5, 10, 20, 30, 40, 50, and 60 minutes of the process, where 0 is the point of light introduction. Degradation efficiency was monitored using a high-performance liquid chromatography system (HPLC, model Shimadzu LC-6A), combined with a photodiode array detector (SPD-M20A) and C18 column (Phenomenex Gemini 5 µm; 150x4.6 mm) working at 45°C. During HPLC measurements mobile phase composed of (v/v) 70% acetonitrile, 29.5% water and 0.5% orthophosphoric acid (85% w/w solution) was used at the flow rate of 0.3 $cm^3 \cdot min^{-1}$. Moreover, mineralization efficiency was analysed after the process as the difference in total organic carbon (TOC) concentration. TOC measurements were performed using Shimadzu TOC-L apparat.

Quantitative analysis of all observed species was performed utilizing the external calibration method using standard compounds, all purchased from Sigma-Aldrich. An HPLC grade acetonitrile and orthophosphoric acid solution were provided by Merck.

2.5. Computational details

The attack of ·OH and $\cdot O_2^-$ radicals on the phenol molecule was studied computationally by calculating the minimum energy path (MEP) of radical addition at the *ortho* and *para* positions. Before MEP calculations, initial and final structures were geometry optimized using DFT calculations with PBE0 hybrid functional and the D3BJ dispersion correction to a convergence threshold of 10^{-8} Ha [38–40]. The MEP calculations were performed using the Nudged Elastic Band (NEB) method with an energy weighted spring constant and L-BFGS optimization method, as implemented in the Orca 4.2.1 software package [41]. In the presented results, the relative 0 energy is a sum of reactants energy obtained in separate runs. Throughout the

calculations, the CPMC model of continuum solvation was introduced to account for the solvent effect during model reactions.

3. Results and discussion

3.1. Structural and morphological analysis

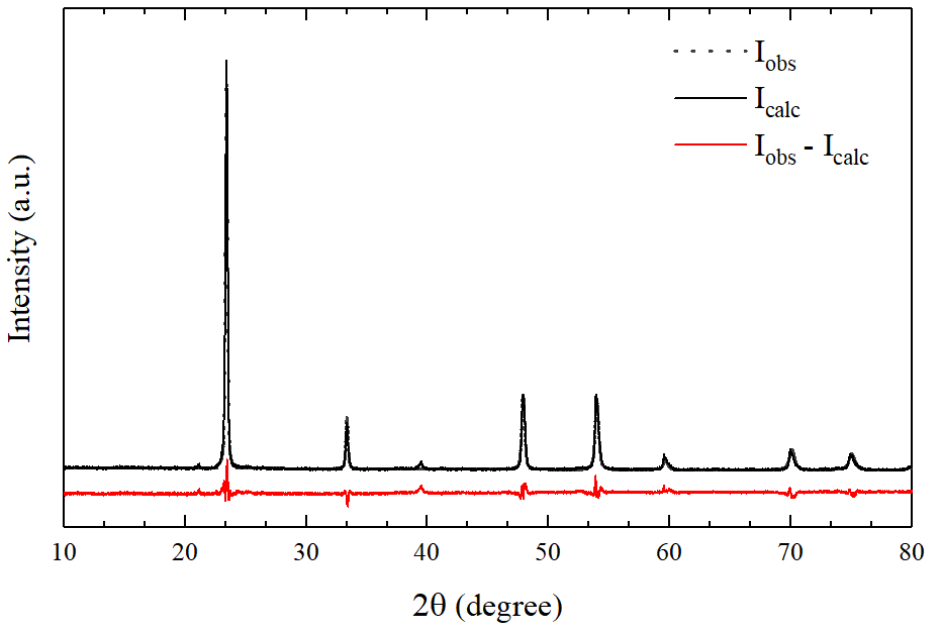

Figure 2. Rietveld refinement of the XRD pattern of the $TiOF_2$ precursor

The phase structure and crystallinity of $TiOF_2$ precursor and TiO_2 nanostructures are significant for their morphologies. Fig. 2 shows the XRD patterns of titanium oxyfluoride compared with the calculated model. All the diffraction peaks corresponding to $TiOF_2$ were observed, which indicates that the $TiOF_2$ with high purity was obtained. The Rietveld refinement was necessary to confirm the presence of titanium oxyfluoride. Therefore, fitting experimental data with the calculated model was performed. The results of Rietveld refinement for the as-obtained TiO_2 nanostructures are presented in Figure S1 and Table S1 in the Supporting Materials.

The broad reflection at $2\theta = 24.3°$ with the highest intensity corresponds to the (100) plane diffraction of $TiOF_2$. As presented in Figure 3, in the second step of the synthesis, the peaks of $TiOF_2$ vanished, and the peak intensity of (101) plane at $2\theta = 25.3^{o}$ of anatase increased,

indicating the complete phase transformation of $TiOF_2$ to anatase. The different environments (1-butanol, hydrofluoric acid, hydrochloric acid, hydrazine hydrate, ammonia water, and water) influenced the shapes of diffraction peak parameters, especially in the range of 2θ = 53-56°. The sample TiO_2_N_2H_4 had the higher reflection at 53.9° than 55° and similar intensities of peaks at 37.8° and 48.1°, which are typical for octahedral TiO_2 nanostructures [6]. The difference between their intensities disappeared in other samples. Titanium(IV) oxide samples prepared by reaction in the presence of acids were more crystallized than obtained in basic conditions. As presented in Table S2 (in the Supporting Materials) the highest amorhous phase content was observed for sample TiO_2_N_2H_4, and the lowest for TiO_2_HF/HCl photocatalyst. No other reflections were detected, suggesting the high purity of the as-synthesized photocatalysts.

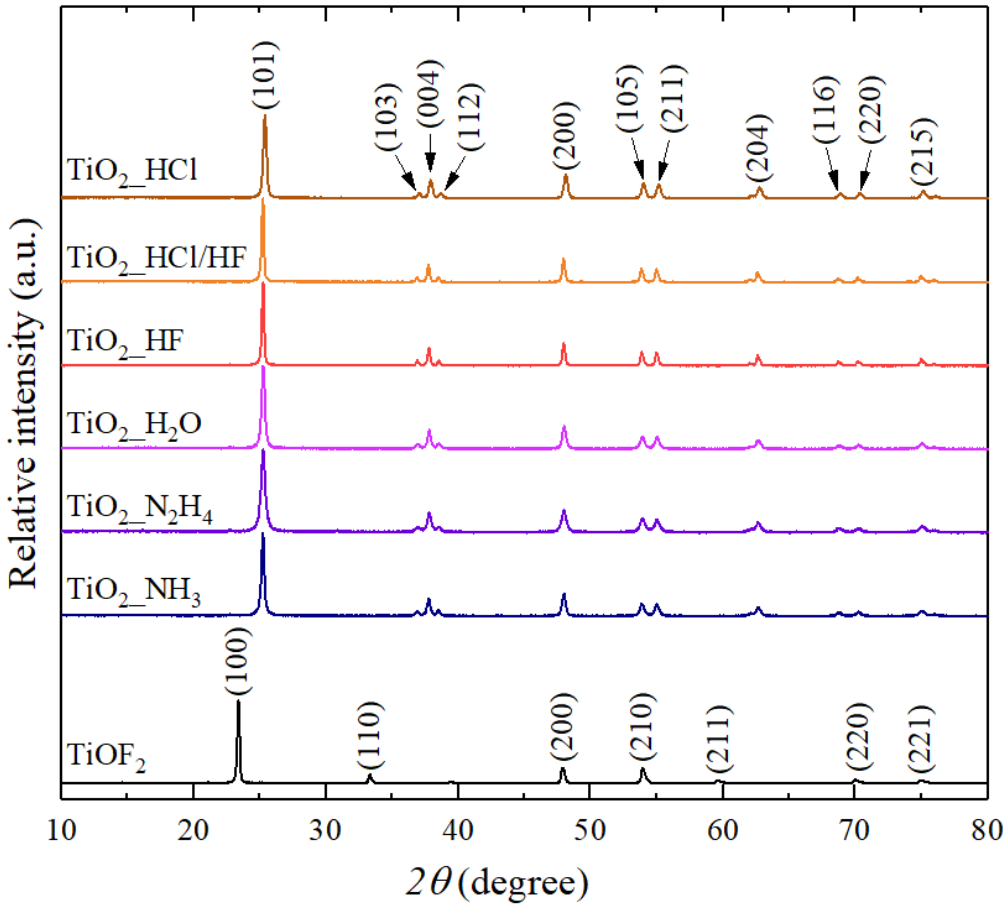

Figure 3. X-ray diffraction patterns of TiO_2 in comparison to the precursor

The XRD pattern of the obtained nanosheets with an observed anatase structure is presented in Figure S2 in the Supporting Materials. The enhancement of the (211) signal, comparing to the (105) one, at approximately 53-55° indicates size reduction along the *c* direction of the anatase structure. It is consistent with reported patterns for anatase nanosheets exposing (001) facets and the effect of HF addition in the alcohol environment [6,18].

The morphologies of $TiOF_2$ precursor and TiO_2 nanostructures were further studied by scanning microscopy analysis. Fig. 4 showed SEM images of the as-prepared $TiOF_2$ powders. It was found that the obtained precursor consists of a mixture of cubic and spherical particles, with a mean size of 260 ± 138 nm (this corresponds to a sphere diameter or a cube side). Comparing to some other results of $TiOF_2$ preparation [27–29,33] the morphology of the obtained precursor is not uniform, which could result from high amounts of TiF_4 used during synthesis. As reported by Wang *et al.*, nanocubic titanium oxyfluoride can be obtained from TiF_4 during the solvothermal alcoholysis process [33]. The final oxidation from fluoride to oxyfluoride results from alcohol condensation and subsequent hydrolysis of initially formed $(RO)_xTiF_{4-x}$ structure. Obtained $TiOF_2$ was observed to form spheres in the first place and was subsequently transformed into cubes as the process was prolonged. Since the kinetics of the described process was reported to depend mostly on H_2O production during alcohol condensation, the conclusion is that a higher amount of TiF_4 to alcohol, would hinder the hydrolysis process, resulting in the formation of both spheres and cubes, as observed. It could probably be managed by increasing reaction time and the introduction of HF, which both include H_2O as a solvent and catalyses alcohol condensation [33]. Nevertheless, in this study, the obtained $TiOF_2$ particles were used as a precursor for the fabrication of TiO_2 nanostructures.

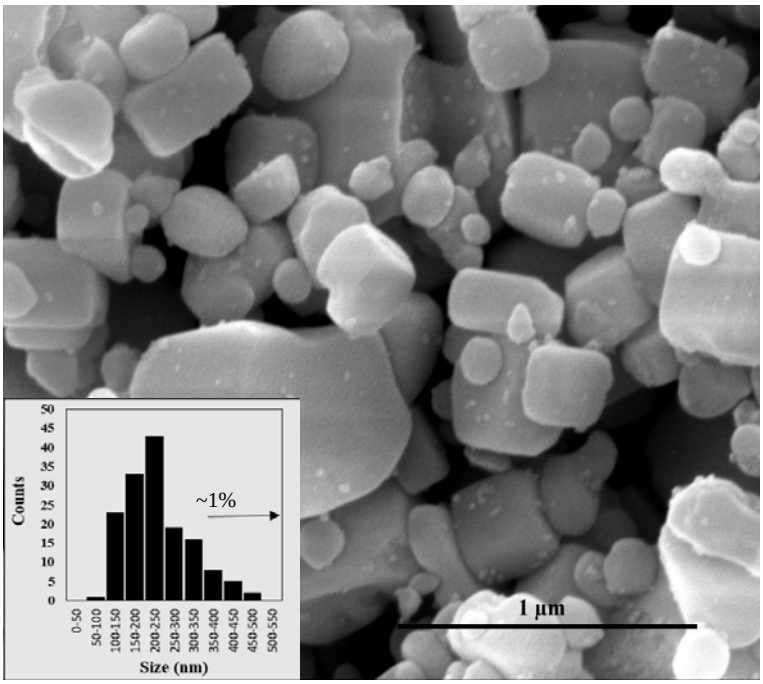

Figure 4. SEM image of $TiOF_2$ precursor

Figures 5 and 6 showed SEM images of the obtained TiO_2, resulting from $TiOF_2$ processing in the presence of different capping agents. In most cases, the formation of clearly defined nanostructures with a size smaller than the original precursor was observed. These primary particles can be freely observed in the sample or are aggregated, forming a representation of the original $TiOF_2$ macroparticle, in a way similar to already observed for TiO_2 hollow boxes obtained from $TiOF_2$ (see in Fig. S3 in the Supporting Materials) [27–29]. It suggests that the initial nucleation of TiO_2 was mostly observed as a surface process, and possible aggregation of the final particles can be controlled by the size reduction of the precursor particles. For fluorinated compounds, the original process is known to result from their hydrolysis, accompanied by HF formation [42], and is followed by a growth of nucleated seeds. The TiO_2 growing is usually described in terms of the rapid dissolution-recrystallization processes [43], in which Ti atoms are reversibly transferred between their solid oxide form and octahedral ions, giving rise to a gradual growth of the specified and most stable crystal structure.

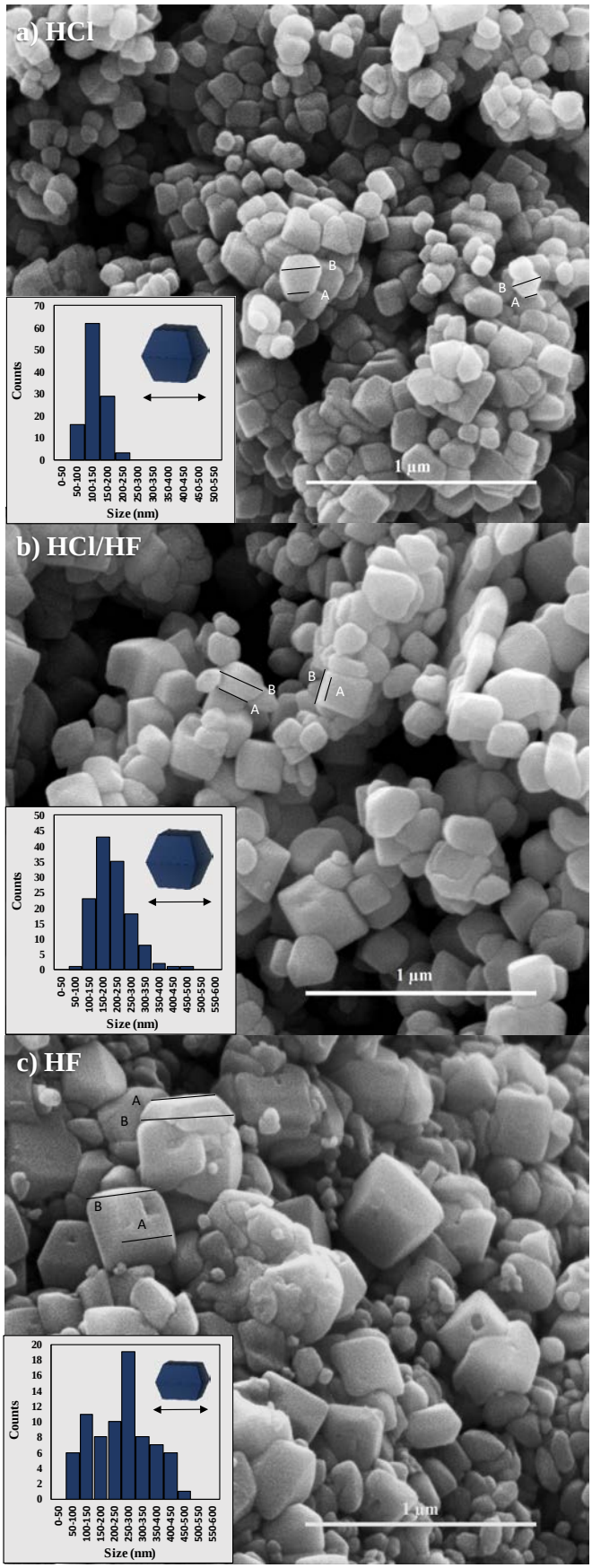

Figure 5. SEM images of TiO_2 samples obtained with addition of a) HCl, b) a mixture of HF and HCl and c) only HF

For a $TiOF_2$ system, without additional substrates, it could be described by a series of following equations (however formation of different octahedrally coordinated Ti species is generally possible [36-37]):

$$TiOF_2 + H_2O \rightarrow TiO_2 + 2HF \quad (1)$$

$$TiO_2 + 4H^+ + 6F^- \rightarrow [TiF_6]^{2-} + 2H_2O \quad (2)$$

$$[TiF_6]^{2-} + 2H_2O \rightarrow TiO_2 + 4H^+ + 6F^- \quad (3)$$

For samples prepared in pure water or acidic environment of HCl or HF, this has led to a formation of anatase decahedrons, enclosed with {001} and {101} facets. These particles can be characterized by a truncation level, defined as a ratio between their top and a middle side (A/B), as highlighted in Figure 5. The final shape of the obtained particles results from competitive growth along both [001] and [101] directions, which depends on their relative surface energy [44]. It is well known that HF presence is crucial for stabilizing {001} surface of anatase [9,16,18], and that is the reason for the highest truncation observed for a sample obtained with the addition of HF during preparation. The observed particles became more enclosed with {101} surface as the environment was changed to HCl/HF and HCl only. For both of these samples, similar morphologies were observed, showing that both acidity and fluorine or chloride presence influenced on the growth behaviour of anatase. It probably results from a mixed effect of a surface protonation [17], increased amounts of molecular HF in the attendance of HCl [45], and their competitive adsorption on the surface of growing particles (HCl is a stronger acid than HF, although also promotes stabilization of {101} surface [6,16]). Moreover, it was observed that increased HF concentration promotes the growth of larger particles, regardless of their truncation.

Comparing with samples obtained at acidic conditions, TiO_2 prepared in pure water was only little truncated and its particles were much smaller. It would be changed when both $N_2H_4 \cdot H_2O$ and $NH_3 \cdot H_2O$ are introduced to the reaction system, resulting in the formation of well-defined

anatase octahedrons and prisms enclosed with {101} pyramids, respectively (see in Fig. 6). Hydrazine was already proved to be an effecting agent for a {101} surface capping and promotes the formation of the octahedral particles when combined with other species stabilizing {001} surface [36]. In this study, the system composed of N_2H_4 and HF could be obtained through hydrazine introduction and initial $TiOF_2$ hydrolysis resulting in the formation of almost completely enclosed octahedrons. These particles can be characterized by some truncation, in a way similar to the previously described HCl/HF samples; however, they are not uniformly enclosed by {001} surface at the top.

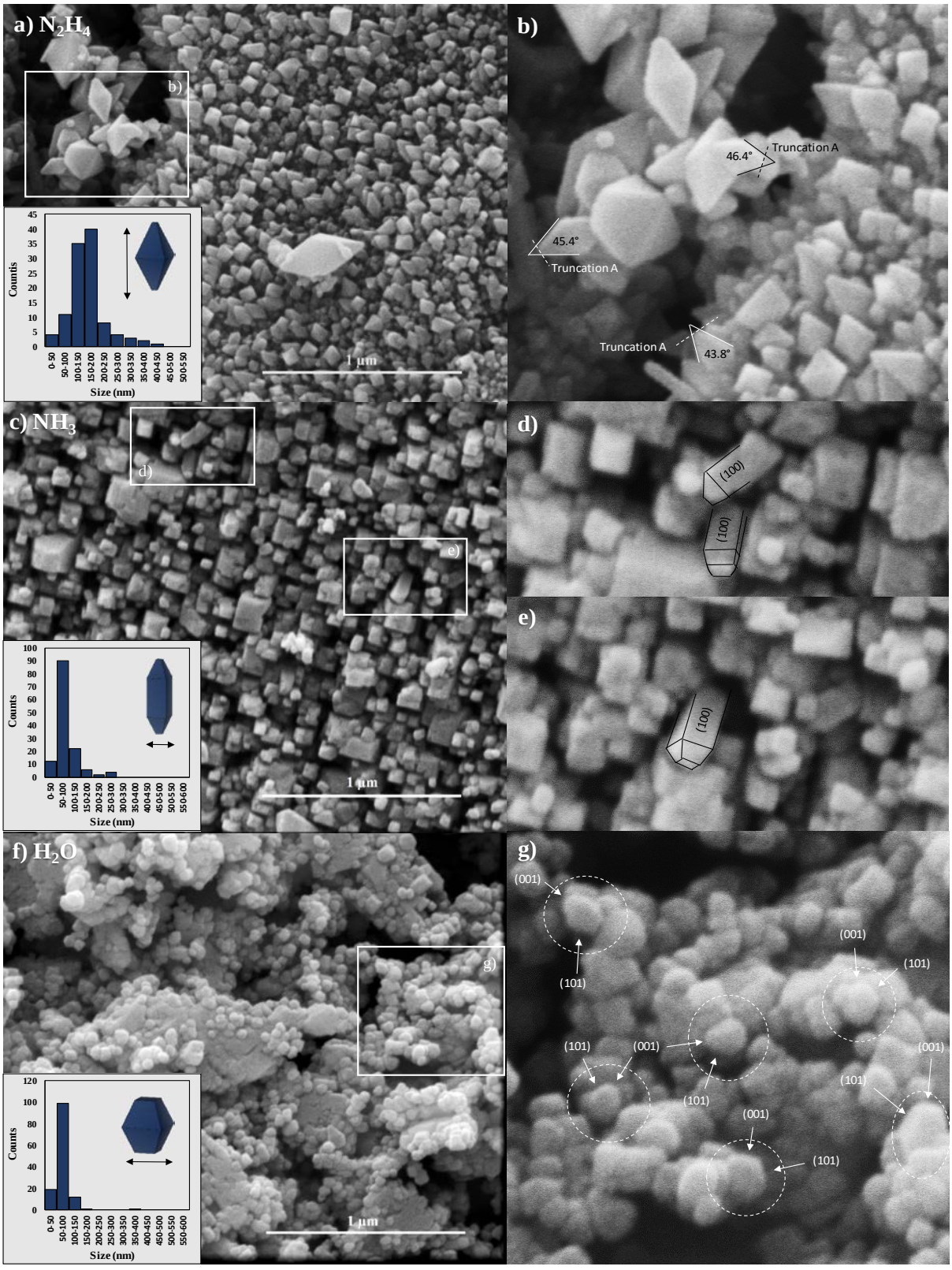

Figure 6. SEM images of TiO_2 samples obtained with addition of a) N_2H_4, c) NH_3 and f) in pure H_2O; b), d), e), g) magnifications of selected areas of a), c), f)

In many cases, a curve, as well as facet, not parallel to a B side, was observed. These could be ascribed to {103} surfaces or a series of microfacets that result in a top curvature [45]. Therefore their nature could differ from these observed in acidic samples [46]. Nevertheless, their content in the total particle's surface was negligible, and they were not analysed in detail. Instead, a simple fact of octahedrons truncation was minded. Finally, a unique morphology was obtained in the presence of NH_3. The formation of elongated rods, with their sides enclosed with anatase {100} and {010} facets was observed, which were topped off with irregular pyramids, composed with a {101}, {001} and possibly other, higher-index facets. Comparing to N_2H_4, ammonium is a stronger base (pK_b = 4.75 for NH_3 versus 5.9 for hydrazine), therefore {100} formation could be explained as the increased basicity of the solution and more oxygenated surface of the growing particles [17]. From SEM images, it was confirmed that simple hydrothermal processing of $TiOF_2$ particles has resulted in the formation of a series of anatase nanostructures, mostly with different ratios of {001} and {101} facets exposition. Moreover, the two-step synthesis starting from TiF_4 enables the formation of fine anatase nanoparticles (mean size between 50-250 nm) rather than macro-sized ones, which are usually obtained from growing directly from titanium fluoride. Nevertheless, particles are mostly aggregated, probably due to the growth on the surface of the precursor (see also in Figure S4 for a macro-sized sample), indicating the critical role of the precursor morphology on the final product. Additionally, the selected area electron diffraction measurements for selected samples were performed, and the results are presented in Figure S5 in the Supporting Materials. The obtained results indicate the presence of all (001), (100) and (101) lattice planes. The (001) and (100) are visible as (004) and (200) reflections due to the extinction rules. However, the observed from SAED analysis patterns were mostly polycrystalline, as shown in Figure S5 with 1, 2 and 3 reflexes corresponding to (101), (004) and (200) respectively.

The performed two-step synthesis from TIF_4 to $TiOF_2$ and subsequently to TiO_2 resulted in a significant size reduction than reported for direct TiF_4 processing [16]. To show a critical effect of the size change on the activity of the obtained photocatalyst the comparison of nanosheets prepared directly from TiF_4 to structures obtained from $TiOF_2$ was performed. The morphology of 2D nanosheets obtained from TiF_4 is shown in Figure S4 in the Supplementary Materials. As expected, the synthesised TiO_2 nanostructures resulted in the formation of a thin macro-sized sheets with highly exposed {001} facets. These particles were partially aggregated forming a flower-like structures.

Measured surface areas of TiO_2 nanostructures are presented in Table 2, together with a summation of the SEM observations. The surface area of the precursor was relatively small, and during the second step of the reaction, this parameter increased for each sample. When the transformation from $TiOF_2$ to TiO_2 occurred, crystal growth started on the surface, and nanocrystals became more textured, smaller, and partially disaggregated in comparison with a precursor, which resulted in the surface development. It is generally followed by an increase in the total pore volume, as shown in Table 2. The specific surface area of TiO_2 nanosheets (see its characteristic in the Supplementary Materials) was 18.1 $m^2 \cdot g^{-1}$, which is generally comparable or higher than TiO_2 nanostructures obtained from $TiOF_2$ to TiO_2 transformation.

Table 2. The representation of the specific surface area and morphology summation of obtained samples. Presented size corresponds to the crystal side highlighted in Figures 5 and 7.

Sample	Surface area [$m^2 \cdot g^{-1}$]	Pore volume [$cm^3 \cdot g^{-1}$]	Mean size [nm]	Crystal shape	Identified facets	Truncation level (A/B)
$TiOF_2$	5.2	0.003	260 ± 138	Spheres and cubes	-	-
TiO_2_HCl	13.8	0.007	132 ± 32	Decahedral	{001}, {101}	0.54 ± 0.09
TiO_2_HCl/HF	9.4	0.006	209 ± 68	Decahedral	{001}, {101}	0.52 ± 0.08
TiO_2_HF	6.1	0.004	250 ± 104	Decahedral	{001}, {101}	0.65 ± 0.08
TiO_2_H_2O	17.2	0.009	74 ± 34	Decahedral	{001}, {101}	0.41 ± 0.07
TiO_2_N_2H_4	33.9	0.017	156 ± 69	Octahedral	{101}	0.17 ± 0.07
TiO_2_NH_3	12.6	0.006	88 ± 32	Rectangular prisms with pyramids on top	{100}, {010}, {101}	-

3.2. X-Ray Photoelectron Spectroscopy

To study the surface composition of the obtained samples X-ray induced photoelectron spectroscopy (XPS) analyses were performed. The survey scans of all samples (Figure S8) confirmed low content of F^- ions (less than 1%) in comparison with other elements, implying their successful removal during post-synthesis treatment and their limited effect on the observed photoactivity. For all samples, the O and Ti signals were dominant. The observed O1s spectra can be resolved into three peaks, which are ascribed to lattice oxygen, bridging oxygen and hydroxyl groups bound to titanium at ~529.2 eV, ~531 eV and ~532.9 eV, respectively [47-48]. Based on the Ti2p XPS spectra (Figure 7), all photocatalysts showed a right shift, which indicates the presence of nonstoichiometric TiO_{2-x} next to TiO_2 compound. The Ti^{3+} sites were not found directly in any sample, which resulted from the oxidizing conditions [49-50].

The content of individual elements was different for the TiO_2 nanostructures. There was observed an overall tendency that the amount of stoichiometric TiO_2 on the surface of the particles decreased at acidic conditions, especially for HF and HF/HCl samples. It followed by the changes in the oxygen species observed at the surface, especially in an increase of Ti-OH and lattice oxygen signals. Observed results correspond with H^+ and HF presence and could be explained as the basis of the HF-induced surface etching. It is known that molecular HF can induce surface decomposition of anatase particles (especially (001) surface), initiated by the substitution of the bridging oxygen by F^- [45]. As the surface bounding of fluorine to titanium is supposed to be occurring in the first place, this process is strongly dependent on the HF amount possible to react with the forming TiO_2. Generally, F^- amounts can be considered as a limiting factor for both particle growth (dissolution/recrystallization reactions 2 and 3) and possible etching. For samples prepared without the addition of HF, it was limited to the F^- introduced through $TiOF_2$ hydrolysis. Therefore, sample $TiO_2\_H_2O$ was obtained in the form of ultrafine particles, which growth was limited due to the small amounts of F^- possible to react

with forming TiO_2. However, the HF formed during the $TiOF_2$ hydrolysis was still able to induce some surface decomposition observed for this sample. Comparing to TiO_2_H_2O, neutralization of HF with hydrazine or ammonia have led to more stoichiometric surface composition and less visible TiO_{2-x} signal. It was changed when HCl was introduced to the system, as the particle growth can be enhanced through the involvement of additional H^+ and Cl^- ions to create $[TiCl_6]^{2-}$. Moreover, in the case of TiO_2_HCl, the F^- amount was still relatively low compared with the Ti presence, which would limit the surface decomposition. It is concluded that such increase in recrystallization efficiency, enabled by the introduction of HCl, together with low content of F^- resulted in the enhancement of particles crystallinity and more stoichiometric surface composition for this sample. Later this is changed when HF was introduced during the synthesis and for samples TiO_2_HF and TiO_2_HCl/HF, enhanced surface etching began with the increase of the TiO_{2-x} signal. Ultimately, the TiO_2_HCl/HF sample was characterized by the highest TiO_{2-x} presence as the hydrochloric acid, having lower pK_a than hydrofluoric acid, enhanced the formation of molecular HF, which is consistent with the observations of Wang *et al.* [45]. Presented surface etching and the relative absence of F^- resulted in the enhanced amount of the surface oxygen, which was introduced to compensate undercoordination of the titanium atoms (e.g., as the oxygen add atoms [51–53]). As shown in Figure 8, the overall ratio of the observed Ti/O changed between approx. 0.35 and 0.24 throughout the samples. The highest values were observed for TiO_2_N_2H_4 and TiO_2_HCl samples and were very close to the expected value of 0.33 (that is, a typical TiO_2 structure with one -OH group attached to every surface Ti atom, with a hypothetical surface formula of TiO_3), while the lowest was observed for both TiO_2_HF and TiO_2_HF/HCl samples, suggesting bounding of the additional oxygens at the surface.

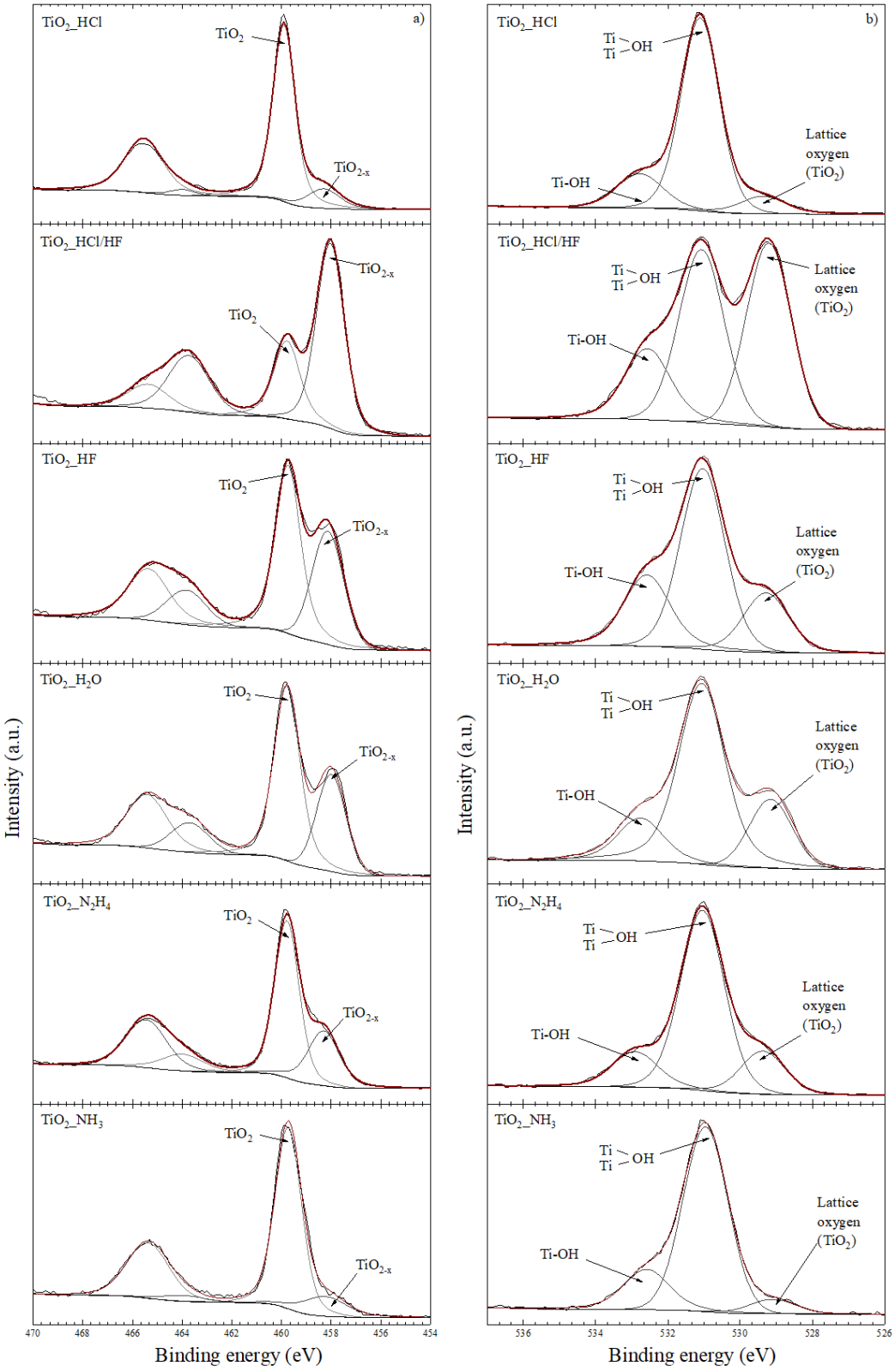

Figure 7. XPS spectra of samples showing a) Ti2p and b) O1s signals with Gaussian fits, respectively

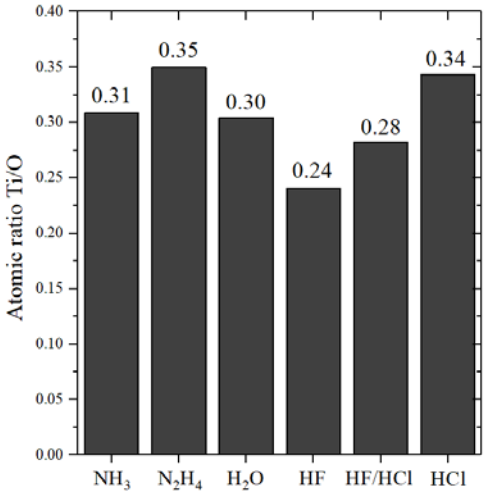

Figure 8. The diagram of atomic ratio Ti/O on the surface for each sample

3.3. Absorption and photoluminescence spectroscopy analysis

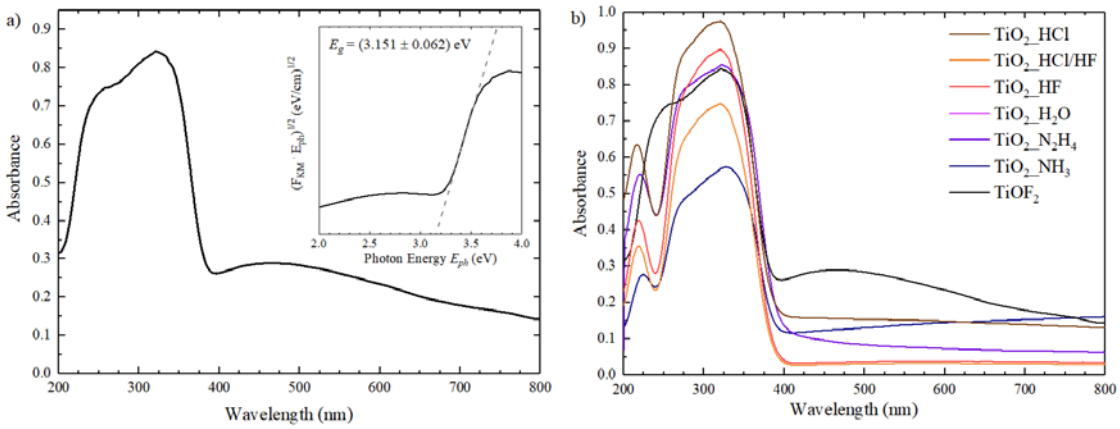

Figure 9. UV-Vis diffuse reflectance spectra of a) $TiOF_2$ and b) TiO_2 nanostructures in comparison with $TiOF_2$. The inset in 9a shows the transformation of Kubelka-Munk function versus photon energy

Fig. 9-a presents the DR-UV-Vis spectra of titanium oxyfluoride. The sample exhibited a considerable absorption below 380 nm range. However, a small band in the range of visible light appears, which vanished for TiO_2 (see Fig. 9-b). This spectrum explains the discrepancy in the literature. Titanium oxyfluoride is shown as a poor photocatalyst [34]. On the other side, Wang et al. [33] presented the small-sized $TiOF_2$ nanocubes with mesoporous structure, which exhibited high activity in the visible light in the reaction of Rhodamine B and 4-chlorophenol degradation. Through the UV–vis spectra, the bandgap of $TiOF_2$ value was (3.15 ± 0.06) eV

was calculated by Tauc method [54]. Energy band gaps for anatase nanostructures are presented in Figure S9 in Supporting Materials.

The photoluminescence (PL) spectra of TiO_2 nanostructures, which were synthesized from $TiOF_2$ were measured at room temperature. The PL spectra of photocatalysts in comparison with the precursor with an excitation wavelength of 250 nm are shown in Figure 10. Four main visible emissions peaks at ~398 nm, ~486 nm, ~528 nm, and ~596 nm were observed. The emission in the UV range describes the band edge emission of the anatase and titanium oxyfluoride, which also explain the bandgap of these materials. The calculated band gaps from the Tauc method were ~3.15 eV for all samples, which correlate with DR-UV-Vis analysis. This band overlaps with bands at ~418 nm and ~443 nm, which originated from the self-trapped excitons localized on the TiO_6 octahedral. Due to the splitting of the conduction band, these types of trapped sites were found below the conduction band edge [55]. The bands at ~486 nm and 596 nm were variously attributed to oxygen vacancies [56]. The 2.55 eV vacancy level, which corresponds to 0.6 eV below the conduction band, has been attributed to Ti^{4+} ions adjacent to oxygen vacancies (intragap surface states). The presence of shallow electron trapping levels located about 0.6−1.6 eV below the conduction band edge is typical for anatase nanostructures [57]. The band at ~ 528 nm is related to non-stoichiometric TiO_2 [55].

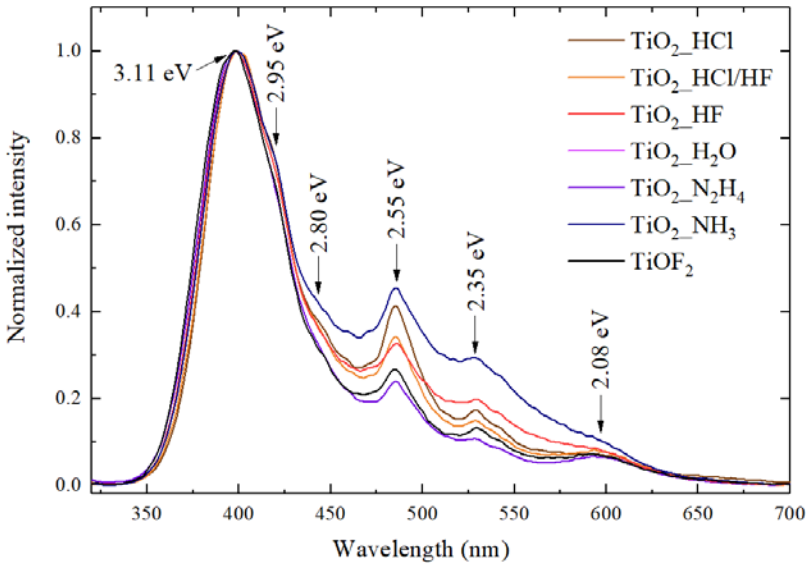

Figure 10. The PL spectra of TiO_2 nanostructures in comparison with $TiOF_2$

3.4. Photocatalytic activity measurements

The photocatalytic activity of TiO_2 nanostructures was studied in a model reaction of phenol degradation. Briefly, photocatalytic oxidation of phenol is known to go through catechol (CT) and hydroquinone (HQ) formation in the first step, followed by their subsequent breaking into series of organic acids (e.g., maleic, fumaric, and oxalic [58–60]), which are finally mineralized to CO_2 and H_2O (see in Fig. 11). Formation of benzoquinone (BQ), being in possible equilibrium with hydroquinone is also mentioned in some works [59–62].

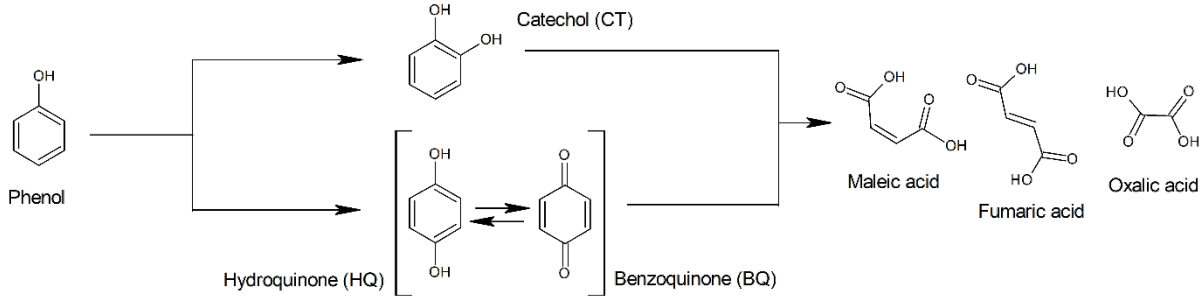

Figure 11. Main mechanism of phenol oxidation during photocatalytic process

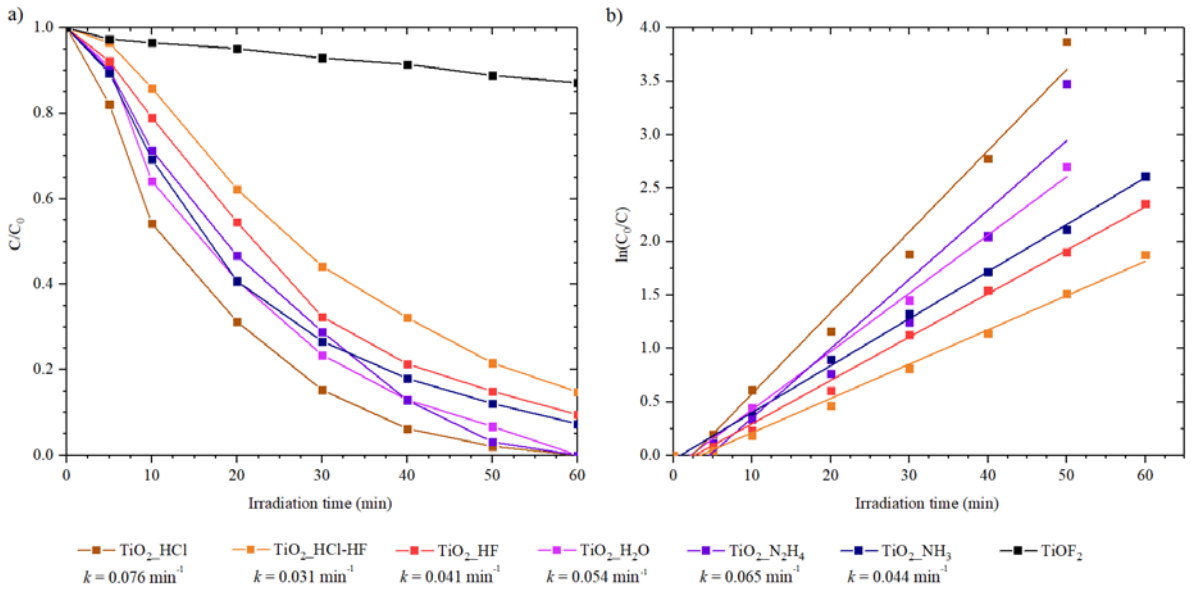

Figure 12. Obtained results of a) phenol degradation for obtained samples and b) their transformation to determine rate constant (assuming first order)

The results of phenol degradation are presented in Figure 12. All samples possessed similar activity, achieving results between 86 and 100% of degradation, while synthesised precursor showed only 13% of phenol disappearance. No clear correlation between their morphology or synthesis conditions alone was found. However, a slight trend to decrease the efficiency for the sample obtained in the presence of HF can be noticed. It can result from a decrease of the surface area and surface defectivity which was observed for these samples. Significantly lower than for the samples prepared from $TiOF_2$ at the same process conditions, phenol degradation efficiency (65% after 1 h of irradiation) was noticed in the presence of the TiO_2 nanosheets obtained from TiF_4, as shown in Figure S10 in the Supporting Materials. Despite rather similar results of phenol removal, obtained materials showed significant differences in mineralization efficiency and formation of oxidation products. Figure 13 show observed phenol removal together with the monitored formation of catechol and hydroquinone for the obtained samples.

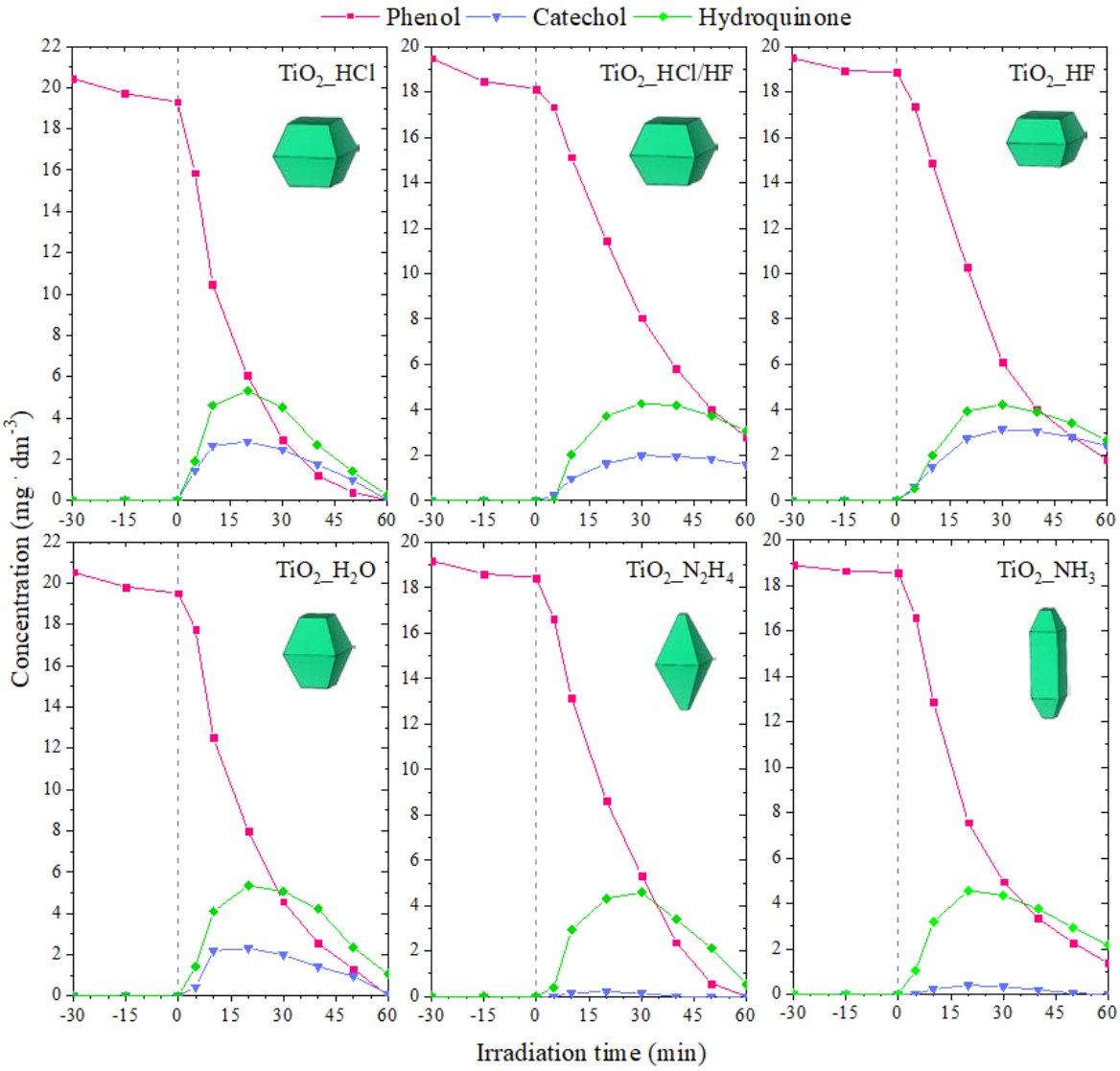

Figure 13. Obtained results of phenol degradation for TiO_2 nanostructures

Within the results, a significant difference in the concentration of *ortho*-hydroxyphenol (catechol) can be observed, while the concentration of hydroquinone is rather similar for all samples. Notably, the lack of defined {001} facets observed for samples TiO_2_NH_3 and TiO_2_N_2H_4 can be correlated to almost the complete disappearance of catechol during the process. After the exclusion of samples TiO_NH_3 (rectangular prisms), the amount of observed CT and HQ was recalculated concerning the amount of decomposed phenol and the results are presented in Figure 14, showing a visible dependence on the {001}/{101} ratio. For photocatalysts with decahedral shape, constant change was observed, and a significant decrease

in catechol concentration was noticed only for octahedrons. It shows the importance of {001} facet presence on the formation of *ortho*-hydroxylated phenol.

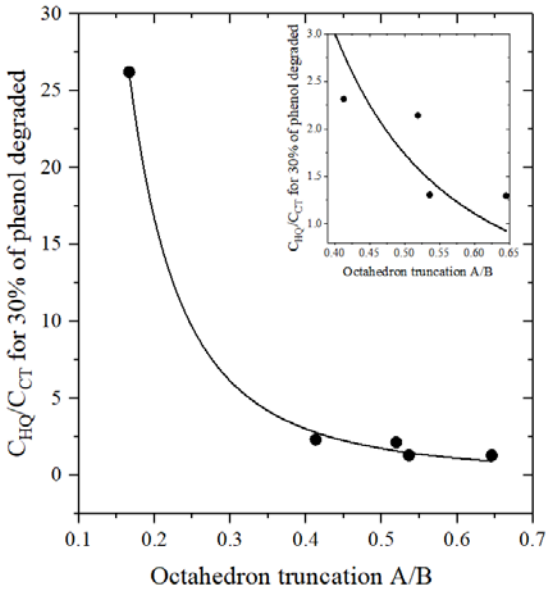

Figure 14. The observed ratio of hydroquinone (HQ) to catechol (CT) formation at the first part of the process with respect to a truncation level.

Moreover, the formation of another aromatic derivative was observed, which was found to be a possible product from BQ ↔ HQ equilibrium. It was analysed by additional irradiation of hydroquinone and benzoquinone solutions in the presence of TiO_2_N_2H_4 and TiO_2_HF samples, both giving rise to a spectrum with characteristic 253 and 374 nm signals. Between them, the TiO_2_HF sample showed a higher formation rate, especially when starting from BQ solution, which is in agreement with the results obtained during phenol runs (see Figure 15-a). Moreover, for BQ stock solution, small amounts of HQ and the described compound were observed already at the start of the process. It can give an idea of the structure of the observed compound. As reported by Kurien and Robins [63], the benzoquinone solutions can spontaneously degrade to 1,2,4-hydroxybenzene or a mixture of 2-hydroxybenzoquinone with HQ. Since, in this study, BQ irradiation gives almost immediate raise to HQ and 253 nm signal, it is concluded that the observed compound is 2-hydroxybenzoquinone (2-HBQ). Described

equilibrium is shown in Figure 15-b, and detailed results of the additional irradiations are shown in Figure S11 in the Supporting Materials.

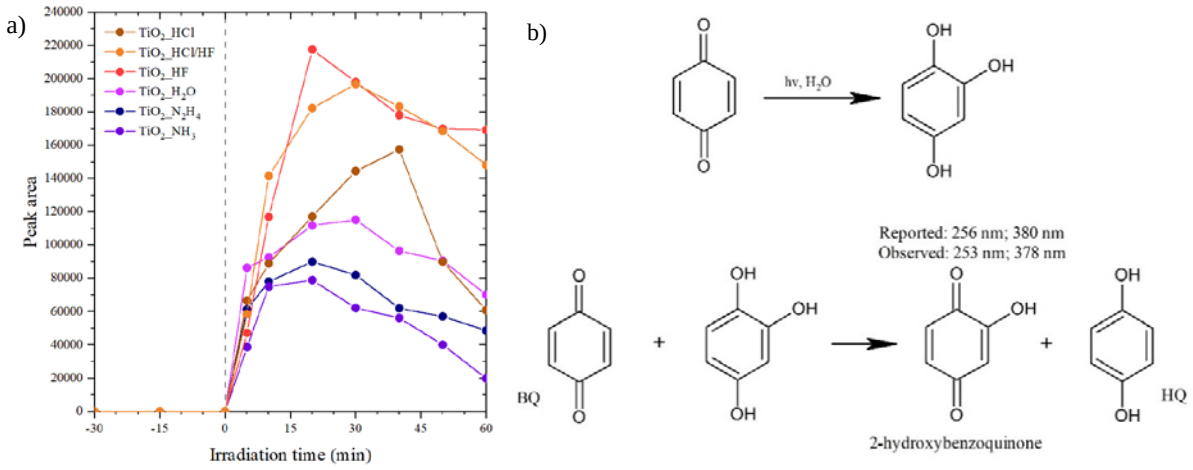

Figure 15. The observed peak area for signal with 253 nm maximum (a) and mechanism of 2hydroxybenzoquinone formation, as reported by Kurien and Robins [63] (b).

A significant difference follows the observed differences in by-products formation and phenol removal in mineralization efficiency. As presented in Figure 16-a, the particles with octahedral shape achieved the highest TOC removal of 78%, while the lowest was observed for the TiO2_HF sample, characterized by the highest truncation ratio. A visible difference between samples TiO_2_N_2H_4 and TiO_2_HCl can be observed, in favour of N_2H_4, suggesting that sample morphology is a more important factor contributing to TOC removal than the simple degradation rate of phenol.

The overall trend of mineralization decreased together with more platelet morphology is well-observed, as shown in Figure 16-b. Analogically to catechol's formation, obtained results create a visible dependence concerning a measured truncation, clearly indicating that nanostructures with less exposed {101} facets are less suitable for phenol mineralization. This change seems to be linear for the obtained samples when grouped in connection with the HF introduction during synthesis and corresponds well with a surface defectivity revealed by the XPS analyses. It is well known that defect type and location can influence TiO_2 activity [64-65], mostly through promoting charge carriers separation or recombination, and generally, one can expect that defects concentration should have some optimal level that supports photocatalyst performance [66–68]. Therefore, it was concluded that increased TiO_{2-x} concentration for HF and HCl/HF samples was mostly responsible for the observed decrease in mineralization efficiency, comparing to other samples. For TiO_2_HCl/HF sample, the morphology is almost the same as for TiO_2_HCl, so the effect of particles shape can be excluded. Moreover, since the sample TiO_2_H_2O also showed considerable amounts of TiO_{2-x}, it could be concluded that the defect formation results in different effect, depending on the surface structure of the sample.

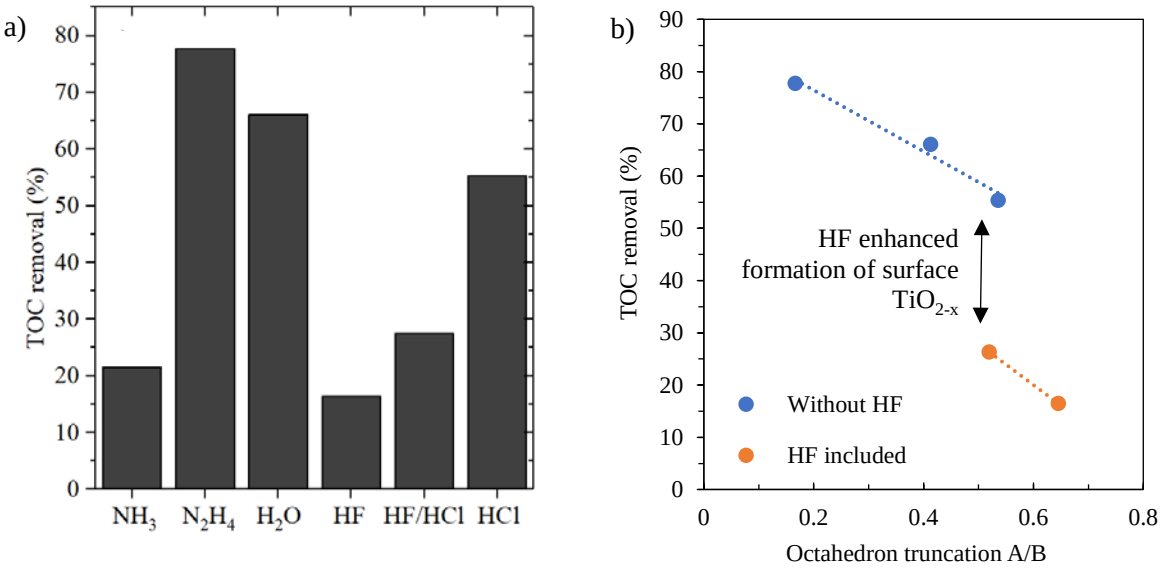

Figure 16. The efficiency of TOC removal for the obtained samples a) and its dependence on the observed truncation level b)

3.5. Degradation mechanism discussion

During the phenol oxidation, the initial reaction provides to form three possible hydroxyl derivatives, distinguished by a type of substitution (*meta*, *ortho,* and *para*). Only compounds in *ortho* (catechol), and *para* (hydroquinone) substitution were observed during degradation experiments. As the first possible factor affecting their formation, generation of different reactive oxygen species (ROS) was considered. In the photocatalytic reactions, ·OH and $\cdot O_2^-$ radicals are most commonly reported to be primary ROS generated at the photocatalyst surface [69–73], so their reactivity with phenol was computationally investigated, as presented in Figure S12 in the Supporting Materials. Figure 16 shows the calculated minimum energy paths of their initial addition to the phenol molecule. The ·OH attack preferentially occurs at the *ortho* position with an energy barrier difference of 10.9 kJ·mol[1] between both isomers. These results correspond well with the electrophilic nature of ·OH and the charge distribution inside phenol molecule, which shows alpha carbons to be more electronegative than *para*-substitution (partial charge of 0.25 versus 0.19, according to Mulliken charge distribution). On the other hand, the $\cdot O_2^-$ attack was also found to occur preferentially at *ortho*-substitution, with a formation of the energetically favourable intermediate state. Moreover, its addition is characterized by a high energy barrier, which could explain existing reports, showing $\cdot O_2^-$ to react slower than ·OH [74].

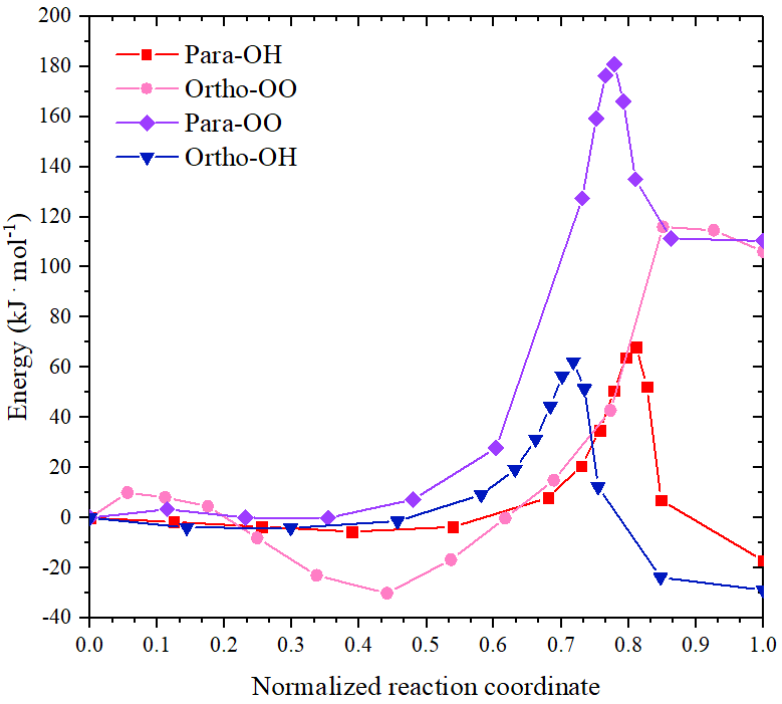

Figure 16. Results of performed NEB calculations of initial ·OH and $\cdot O_2^-$ attack on different patterns in phenol molecule

The obtained computational results can support the experimental observations of increased catechol formation for samples more exposed with {001} facets. As shown by Ma et al., the photogenerated holes tend to localize at the bridging oxygens of (001) surface, while electrons remain in bulk-localized Ti atoms [75]. Moreover, the (001) surface in comparison with (101) and (100) is the only one with a high density of low energy O 2s states above the valence band edge of the TiO_2 [76]. Therefore, it is suitable for the oxidation of H_2O to ·OH. The preference of {001} facets to create ·OH though hole trapping on the surface bridging O would also explain the significant effect of TiO_{2-x} formation on the activity of more truncated samples (HF and HF/HCl). On the other hand, the (101) surface is adequate for electrons accumulation and should promote oxygen reduction to $\cdot O_2^-$. It is in accordance with our study, as the superoxide radicals were reported to be very effective ring-opening agents [77]. Therefore, their enhanced generation could explain high TOC removal by the {101} exposing particles, while observed phenol removal rate is similar, because of the high energy barrier of their initial addition.

Nevertheless, the obtained results cannot fully explain experimental observations, mostly regarding the disappearance of catechol for the particles exposed only with {101} facets. It suggests that surface effects must also influence on the degradation mechanism. In this case, some geometric consideration can be taken into account. As shown in Figure 17, the phenol adsorption at the TiO_2 surface should occur between -OH moiety and the Ti sites, acting as the Lewis acid, which for (001) leaves four twofold-coordinated oxygens in the direct neighbourhood of the adsorbed phenol. Such increase of the density of surface oxygens, close to Ti (1.98 Å away) should promote ·OH attack at *ortho* substitution and can also explain the increased formation of the 2hydroxybenzoquinone, resulting from further hydroxylation of BQ or HQ.

On the other hand, the oxygen reduction at the TiO_2 surface, preferentially (101), should also occur at the Ti site, which results in a higher distance between both reactants. Starting from the phenol-adsorbed Ti atom, the closest Ti site is 3.79 Å away, while the bond length between *ipso* and *ortho* carbons is 1.39 Å. Therefore, it is suggested that the increased Ti-Ti distance at the surface could prevent *ortho* substitution of $\cdot O_2^-$, which could be especially valid for (101) surface due to its preference to accumulate electrons on the surface Ti atoms. These results suggest that photocatalyst structure can promote a specific pathway of the degradation of the pollutants and could be an important factor considering the oxidation of more complex compounds, such as pharmaceuticals, pesticides or dyes.

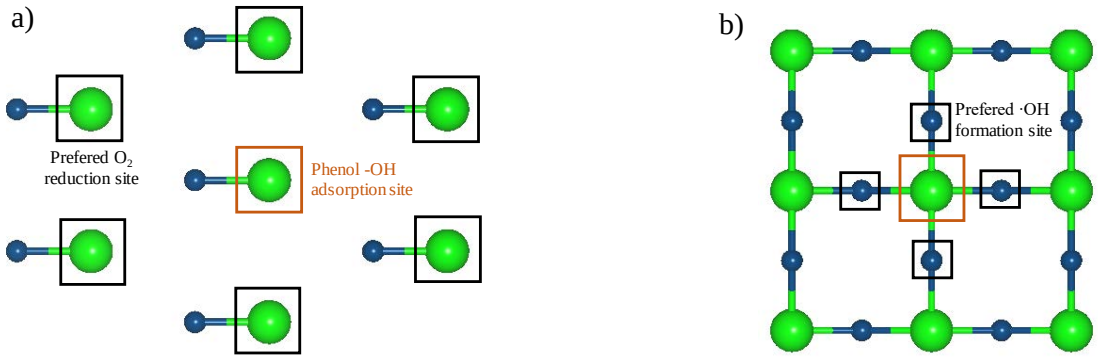

Figure 17. Simplified view on the top of anatase surface, showing undercoordinated Ti and O atoms around hypothetical site of phenol -OH adsorption: a) (101) and b) (001) surface. In the squares, there are highlighted sites which are expected to be especially active for this surface

4. Conclusions

To summarize, a simple synthetic method for the synthesis of TiO_2 nanostructures by a solvothermal route from the $TiOF_2$ precursor was developed. Different environments of reactions (acidic/basic) and capping agents were studied, showing that the application of titanium oxyfluoride allows obtaining TiO_2 nanostructures with various morphologies (decahedral, octahedral, rectangular prisms). Shapes of nanostructures were related to exposed facets, which were crucial concerning the mineralization efficiency and the pathway of phenol degradation. The TiO_2 octahedral particles exposing {101} facets exhibited the highest TOC removal efficiency under UV light irradiation, which decreased as the other facets appeared and became more exposed to the surface of the particles. Experimental results were confronted with simulated ·OH and $\cdot O_2^-$ attack on a phenol molecule, showing that the ·OH addition at the *ortho* substitution is energetically favoured. It explains the importance of {001} facet for the enhanced formation of catechol as the photogenerated holes, as opposed to electrons, are expected to preferential localize on this plane. On the other hand, the increased formation of $\cdot O_2^-$ on the {101} facet was expected because of the significant effect of {101} exposition on TOC reduction and favoured electron localization on the surface. However, the direct attack of

$\cdot O_2^-$ on the phenol molecule cannot provide a mechanism for occurring reaction and cannot explain the formation of *para*-substituted products. Based on the increased distance between neighbouring sites that could promote superoxide radical attack at the *para* position, it was suggested that surface structure might be another factor contributing to the creation of the products.

Funding: The research was financially supported by Polish National Science Centre (Grant No. NCN 2018/30/E/ST5/00845).

Acknowledgements

The research was financially supported by Polish National Science Centre (Grant No. NCN 2018/30/E/ST5/00845) and Polish Ministry of Science and Higher Education grant no. 0525/E-359/STYP/13/2018 Scholarships for outstanding young scientists.

References

[1] A. Umar, F. A. Harraz, A. A. Ibrahim, T. Almas, R. Kumar, M. S. Al-Assiri, and S. Baskoutas, *Coatings*, 2020, **10**, 182.

[2] A. Umar, M. S. Akhtar, R. I. Badran, M. Abaker, S. H. Kim, A. Al-Hajry, and S. Baskoutas, *Applied Physics Letters*, 2013, **103**.

[3] J. Li, Y. Lu, Z. Wu, Y. Bao, R. Xiao, H. Yu, and Y. Chen, *Ceramics International*, 2016, **42**, 9621.

[4] G. Xiang, Z. Yu, Y. Hou, Y. Chen, Z. Peng, L. Sun, and L. Sun, *Separation and Purification Technology*, 2016, **161**, 144.

[5] C. Günnemann, C. Haisch, M. Fleisch, J. Schneider, A. V. Emeline, and D. W. Bahnemann, *ACS Catalysis*, 2019, **9**, 1001.

[6] T. R. Gordon, M. Cargnello, T. Paik, F. Mangolini, R. T. Weber, P. Fornasiero, and C. B. Murray, *Journal of the American Chemical Society*, 2012, **134**, 6751.

[7] W. J. I. DeBenedetti, E. S. Skibinski, D. Jing, A. Song, and M. A. Hines, *Journal of*

Physical Chemistry C, 2018, **122**, 4307.

[8] Y. Wang, H. Sun, S. Tan, H. Feng, Z. Cheng, J. Zhao, A. Zhao, B. Wang, Y. Luo, J. Yang, and J. G. Hou, *Nature Communications*, 2013, **4**, 1.

[9] C. Z. Wen, J. Z. Zhou, H. B. Jiang, Q. H. Hu, S. Z. Qiao, and H. G. Yang, *Chemical Communications*, 2011, **47**, 4400.

[10] M. Zhang, X. Xiao, X. Wang, M. Chen, Y. Lu, M. Liu, and L. Chen, *Nanoscale*, 2019, **11**, 7465.

[11] Z. Wei, M. Janczarek, M. Endo, K. Wang, A. Balčytis, A. Nitta, M. G. Méndez-Medrano, C. Colbeau-Justin, S. Juodkazis, B. Ohtani, and E. Kowalska, *Applied Catalysis B: Environmental*, 2018, **237**, 574.

[12] Y. Lu, Y. Zang, H. Zhang, Y. Zhang, G. Wang, and H. Zhao, *Science Bulletin*, 2016, **61**, 1003.

[13] X. Zhao, W. Jin, J. Cai, J. Ye, Z. Li, Y. Ma, J. Xie, and L. Qi, *Advanced Functional Materials*, 2011, **21**, 3554.

[14] J. Mao, L. Ye, K. Li, X. Zhang, J. Liu, T. Peng, and L. Zan, *Applied Catalysis B: Environmental*, 2014, **144**, 855.

[15] Y. Liang, Y. Yang, H. Zhou, C. Zou, K. Xu, X. Luo, T. Yu, W. Zhang, Y. Liu, and C. Yuan, *Ceramics International*, 2019, **45**, 6282.

[16] H. G. Yang, C. H. Sun, S. Z. Qiao, J. Zou, G. Liu, S. C. Smith, H. M. Cheng, and G. Q. Lu, *Nature*, 2008, **453**, 638.

[17] A. S. Barnard and L. A. Curtiss, *Nano Letters*, 2005, **5**, 1261.

[18] M. Li, Y. Chen, W. Li, X. Li, H. Tian, X. Wei, Z. Ren, and G. Han, *Small*, 2017, **13**.

[19] Y. Zheng, J. Wang, and P. Yang, *Journal of Nanoscience and Nanotechnology*, 2017, **17**, 1204.

[20] N. Wu, J. Wang, D. N. Tafen, H. Wang, J. Zheng, J. P. Lewis, X. Liu, and S. S.

Leonard, *Journal of Americal Chemical Society*, 2010, **2**, 6679.

[21] D. Wang, J. Liu, Q. Huo, Z. Nie, W. Lu, R. E. Williford, and Y. B. Jiang, *Journal of the American Chemical Society*, 2006, **128**, 13670.

[22] J. Li, Y. Yu, Q. Chen, J. Li, and D. Xu, *Crystal Growth and Design*, 2010, **10**, 2111.

[23] N. M. Laptash and I. G. Maslennikova, *Advances in Materials Physics and Chemistry*, 2012, **02**, 21.

[24] A. A. Andreev and A. N. Diachenko, *Theoretical Foundations of Chemical Engineering*, 2009, **43**, 707.

[25] V. I. Sachkov, R. A. Nefedov, V. V. Orlov, R. O. Medvedev, and A. S. Sachkova, *Minerals*, 2018, **8**, 1.

[26] J. Hu, Y. Cao, K. Wang, and D. Jia, *RSC Advances*, 2017, **7**, 11827.

[27] Y. Zheng, X. Hu, and P. Yang, *CrystEngComm*, 2018, **20**, 4485.

[28] C. Z. Wen, Q. H. Hu, Y. N. Guo, X. Q. Gong, S. Z. Qiao, and H. G. Yang, *Chemical Communications*, 2011, **47**, 6138.

[29] Z. Huang, Z. Wang, K. Lv, Y. Zheng, and K. Deng, *ACS Applied Materials and Interfaces*, 2013, **5**, 8663.

[30] B. Li, D. Wang, Y. Wang, B. Zhu, Z. Gao, Q. Hao, Y. Wang, and K. Tang, *Electrochimica Acta*, 2015, **180**, 894.

[31] N. Louvain, Z. Karkar, M. El-Ghozzi, P. Bonnet, K. Guérin, and P. Willmann, *Journal of Materials Chemistry A*, 2014, **2**, 15308.

[32] J. Zhu, F. Lv, S. Xiao, Z. Bian, G. Buntkowsky, C. Nuckolls, and H. Li, *Nanoscale*, 2014, **6**, 14648.

[33] J. Wang, F. Cao, Z. Bian, M. K. H. Leung, and H. Li, *Nanoscale*, 2014, **6**, 897.

[34] Z. Wang, K. Lv, G. Wang, K. Deng, and D. Tang, *Applied Catalysis B: Environmental*, 2010, **100**, 378.

[35] A. Ballestas-Barrientos, X. Li, S. Yick, A. F. Masters, and T. Maschmeyer, *Sustainable Energy and Fuels*, 2018, **2**, 1463.

[36] L. Gai, Q. Mei, X. Qin, W. Li, H. Jiang, and X. Duan, *Materials Research Bulletin*, 2013, **48**, 4469.

[37] P. Leidich, O. Linker, M. Panthöfer, and W. Tremel, *CrystEngComm*, 2014, **16**, 8486.

[38] S. Grimme, J. Antony, S. Ehrlich, and H. Krieg, *Journal of Chemical Physics*, 2010, **132**.

[39] C. Adamo and V. Barone, *Journal of Chemical Physics*, 1999, **110**, 6158.

[40] J. P. Perdew, M. Ernzerhof, K. Burke, J. P. Perdew, M. Ernzerhof, and K. Burke, 2010, **9982**, 9982.

[41] F. Neese, *Wiley Interdisciplinary Reviews: Computational Molecular Science*, 2012, **2**, 73.

[42] J. C. Lytle, H. Yan, R. T. Turgeon, and A. Stein, *Chemistry of Materials*, 2004, **16**, 3829.

[43] Y. Chen, W. Li, J. Wang, Y. Gan, L. Liu, and M. Ju, *Applied Catalysis B: Environmental*, 2016, **191**, 94.

[44] R. Li, X. Zhang, H. Dong, Q. Li, Z. Shuai, and W. Hu, *Advanced Materials*, 2016, **28**, 1697.

[45] Y. Wang, H. Zhang, Y. Han, P. Liu, X. Yao, and H. Zhao, *Chemical Communications*, 2011, **47**, 2829.

[46] G. Fazio, D. Selli, L. Ferraro, G. Seifert, and C. Di Valentin, *ACS Applied Materials and Interfaces*, 2018, **10**, 29943.

[47] X. Chen, Y. Cui, X. Yan, L. Tian, and X. Chen, *Black TiO 2 Nanomaterials for Energy Applications* , 2017, 5.

[48] T. Leshuk, R. Parviz, P. Everett, H. Krishnakumar, R. A. Varin, and F. Gu, *ACS*

Applied Materials and Interfaces, 2013, **5**, 1892.

[49] Y. Zhang, X. Wang, P. Dong, Z. Huang, X. Nie, and X. Zhang, *Green Chemistry*, 2018, **20**, 2084.

[50] A. Zielińska-jurek, Z. Wei, M. Janczarek, I. Wysocka, and E. Kowalska, *Catalysts*, 2019, **9**, 1.

[51] J. P. C. C, Y. Du, Z. Dohna, and I. Lyubinetsky, *Journal of Physical Chemistry C*, 2008, **2**, 2649.

[52] Y. Wang, D. Pillay, and G. S. Hwang, *Physical Review B - Condensed Matter and Materials Physics*, 2004, **70**, 1.

[53] Q. Zhang, Y. J. Li, H. F. Wen, Y. Adachi, M. Miyazaki, Y. Sugawara, R. Xu, Z. H. Cheng, J. Brndiar, L. Kantorovich, and I. Štich, *Journal of the American Chemical Society*, 2018, **140**, 15668.

[54] J. Tauc, R. Grigorovici, and A. Vancu, *Physica Status Solidi (B) Basic Research*, 1966, **627**, 363.

[55] G. Nabi, W. Raza, and M. B. Tahir, *Journal of Inorganic and Organometallic Polymers and Materials*, 2019, **30**, 1425.

[56] M. M. Kumar, S. Badrinarayanan, and M. Sastry, *Thin Solid Films*, 2000, **358**, 122.

[57] A. Fujishima, X. Zhang, and D. A. Tryk, *Surface Science Reports*, 2008, **63**, 515.

[58] A. Turki, C. Guillard, F. Dappozze, Z. Ksibi, G. Berhault, and H. Kochkar, *Applied Catalysis B: Environmental*, 2015, **163**, 404.

[59] A. Sobczyński, L. Duczmal, and W. Zmudziński, *Journal of Molecular Catalysis A: Chemical*, 2004, **213**, 225.

[60] L. G. Devi and K. E. Rajashekhar, *Journal of Molecular Catalysis A: Chemical*, 2011, **334**, 65.

[61] T. T. T. Dang, S. T. T. Le, D. Channei, W. Khanitchaidecha, and A. Nakaruk, *Research*

on Chemical Intermediates, 2016, **42**, 5961.

[62] I. Wysocka, E. Kowalska, K. Trzciński, M. Łapiński, G. Nowaczyk, and A. Zielińska-Jurek, *Nanomaterials*, 2018, **8**.

[63] K. C. Kurien and P. A. Robins, *Journal of the Chemical Society B: Physical Organic*, 1970, 855.

[64] Y. Nam, L. Li, J. Y. Lee, and O. V. Prezhdo, *Journal of Physical Chemistry Letters*, 2019, **10**, 2676.

[65] M. Kong, Y. Li, X. Chen, T. Tian, P. Fang, F. Zheng, and X. Zhao, *Journal of Am*, 2011, **133**, 16414.

[66] C. Liu, A. Y. Zhang, D. N. Pei, and H. Q. Yu, *Environmental Science and Technology*, 2016, **50**, 5234.

[67] M. Liu, H. Li, and W. Wang, *Catalysis Today*, 2016, **264**, 236.

[68] T. Nakano, R. Ito, S. Kogoshi, and N. Katayama, *Journal of Physics and Chemistry of Solids*, 2016, **98**, 136.

[69] E. Jimenez-Relinque and M. Castellote, *Applied Catalysis A: General*, 2018, **565**, 20.

[70] F. Dong, T. Xiong, Y. Sun, L. Lu, Y. Zhang, H. Zhang, H. Huang, Y. Zhou, and Z. Wu, *Applied Catalysis B: Environmental*, 2017, **219**, 450.

[71] R. Nakamura, T. Okamura, N. Ohashi, A. Imanishi, and Y. Nakato, *Journal of Americal Chemical Society*, 2005, **127**, 12975.

[72] W. Jiang, J. A. Joens, D. D. Dionysiou, and K. E. O'Shea, *Journal of Photochemistry and Photobiology A: Chemistry*, 2013, **262**, 7.

[73] K. Lv, X. Guo, X. Wu, Q. Li, W. Ho, M. Li, H. Ye, and D. Du, *Applied Catalysis B: Environmental*, 2016, **199**, 405.

[74] D. W. Bahnemann, M. Hilgendorff, and R. Memming, *Journal of Physical Chemistry A*, 1997, **101**, 4265.

[75] X. Ma, Y. Dai, M. Guo, and B. Huang, *Langmuir*, 2013, **29**, 13647.

[76] Z. Zhao, Z. Li, and Z. Zou, *Journal of Physics Condensed Matter*, 2010, **22**.

[77] C. S. A. Antunes, M. Bietti, M. Salamone, and N. Scione, *Journal of Photochemistry and Photobiology A: Chemistry*, 2004, **163**, 453.

Supporting Information

Facet effect of TiO_2 nanostructures from $TiOF_2$ and their photocatalytic activity

Marta Kowalkińska[1], Szymon Dudziak[1], Jakub Karczewski[2], Jacek Ryl[3], Grzegorz Trykowski[4], Anna Zielińska-Jurek[1*]

[1] Department of Process Engineering and Chemical Technology, Faculty of Chemistry, Gdansk University of Technology (GUT), G. Narutowicza 11/12, 80-233 Gdańsk, Poland

[2] Department of Solid State Physics, Faculty of Applied Physics and Mathematics, Gdansk University of Technology (GUT), 80-233 Gdańsk, Poland

[3] Department of Electrochemistry, Corrosion and Materials Engineering, Gdansk University of Technology (GUT), 80-233 Gdańsk, Poland

[4]Faculty of Chemistry, Nicolaus Copernicus University, Gagarina 7, 87-100 Toruń, Poland

* Corresponding author: annjurek@pg.edu.pl

1. Results

1.1. X-Ray diffraction of the obtained samples

Fig. S1 shows the XRD patterns of obtained products after the Rietveld refinement. The fitting experimental data with the calculated model was successful. The results of Rietveld refinement are presented in Table S1. The estimation of the size of anatase crystallites along (101) plane was performed based on the Scherrer formula.

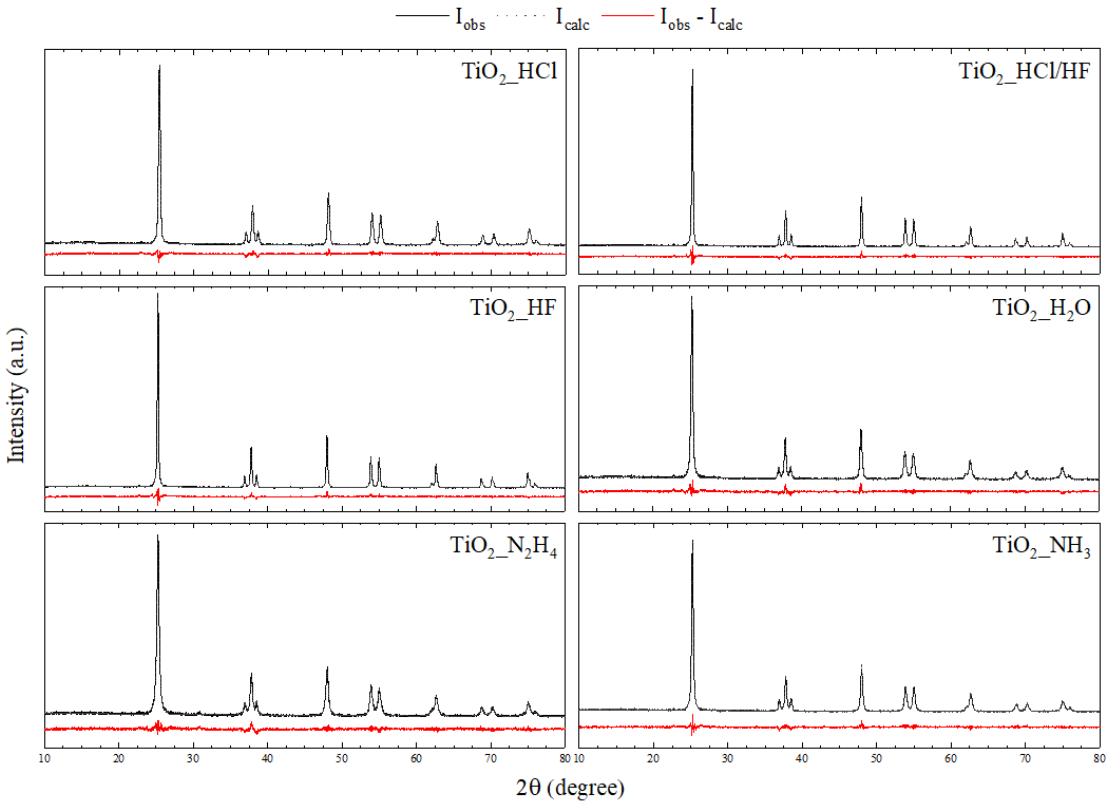

Figure S1. Rietveld refinement of the XRD pattern of the TiO_2 nanostructures

Table S1. Microstructural parameters of TiO_2 nanostructures and precursor obtained by XRD analysis.

Sample name	Crystallite size [nm]	Lattice parameters [Å]		Rietveld parameters		
		a,b	c	R_{exp}	R_{wp}	χ^2
$TiOF_2$	63.61	3.794	-	9.068	15.274	2.837
TiO_2_NH_3	32.84	3.786	9.506	9.397	11.985	1.627
TiO_2_N_2H_4	20.25	3.788	9.505	9.157	11.821	1.666
TiO_2_H_2O	28.46	3.788	9.509	9.297	12.045	1.696
TiO_2_HF	55.17	3.788	9.509	6.372	10.067	2.496
TiO_2_HF/HCl	51.44	3.787	9.511	6.691	9.952	2.213
TiO_2_HCl	30.18	3.789	9.515	7.178	9.148	1.625
TiO_2_onestep	32.81	3.788	9.507	6.568	11.827	3.242

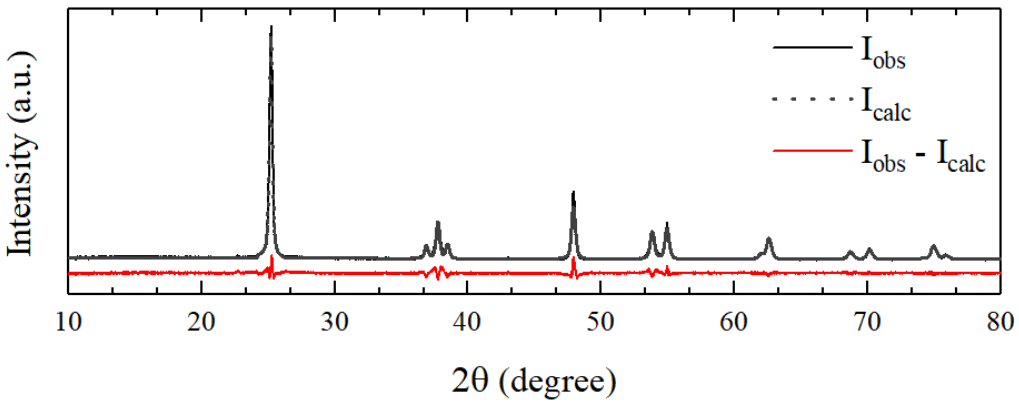

Figure S2. XRD pattern of the TiO_2 sheets, obtained from TiF_4 in the presence of HF.

Crystallinity of the obtained samples was analyzed using NiO as the internal standard and the content of amorphous phase was calculated from the difference between NiO content and the value indicated from XRD. The obtained results are presented in Table S2.

Table S2. Calculated contents of amorphous phase.

Sample name	TiO_2_NH_3	TiO_2_N_2H_4	TiO_2_H_2O	TiO_2_HF	TiO_2_HF/HCl	TiO_2_HCl
Amorphous phase [weight %]	32	44	31	16	7	18

1.2. Morphology

Figure S3 shows the morphology of macro-sized aggregate spotted during TiO_2_NH_3 sample observations. The cubic macroparticle preserved the shape of the initial precursor with visible TiO_2 particles formed on the surface and a partial disaggregation observed between neighbouring sides of the cube. These observations are similar to the reported transformation of $TiOF_2$ into TiO_2 hollow nanoboxes, which could be further decomposed to nanosheets [25-26]. It proves that $TiOF_2$ hydrolysis, and subsequent TiO_2 nucleation occur on the precursor's surface, and the reaction environment controls only further TiO_2 growth. The surface-controlled character of the ongoing process can explain why only an extremely big cube aggregate is observed, as the smaller $TiOF_2$ particles would be converted to TiO_2 and subsequently dissociated faster than the big ones. Therefore, it shows an important role of the $TiOF_2$

morphology on the described transformation. The higher magnification of the TiO_2 particles is shown in the main text.

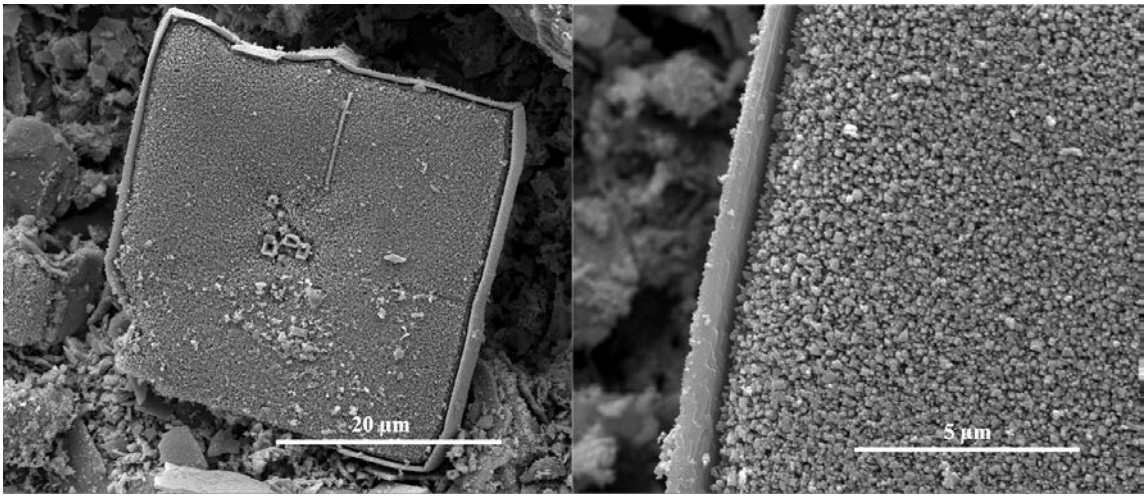

Figure S3. SEM images of TiO_2 aggregate spotted during TiO_2_NH_3 observations

The performed two-step synthesis from TIF_4 to $TiOF_2$ and subsequently to TiO_2 resulted in a significant size reduction than reported for direct TiF_4 processing, see in Figure S4.

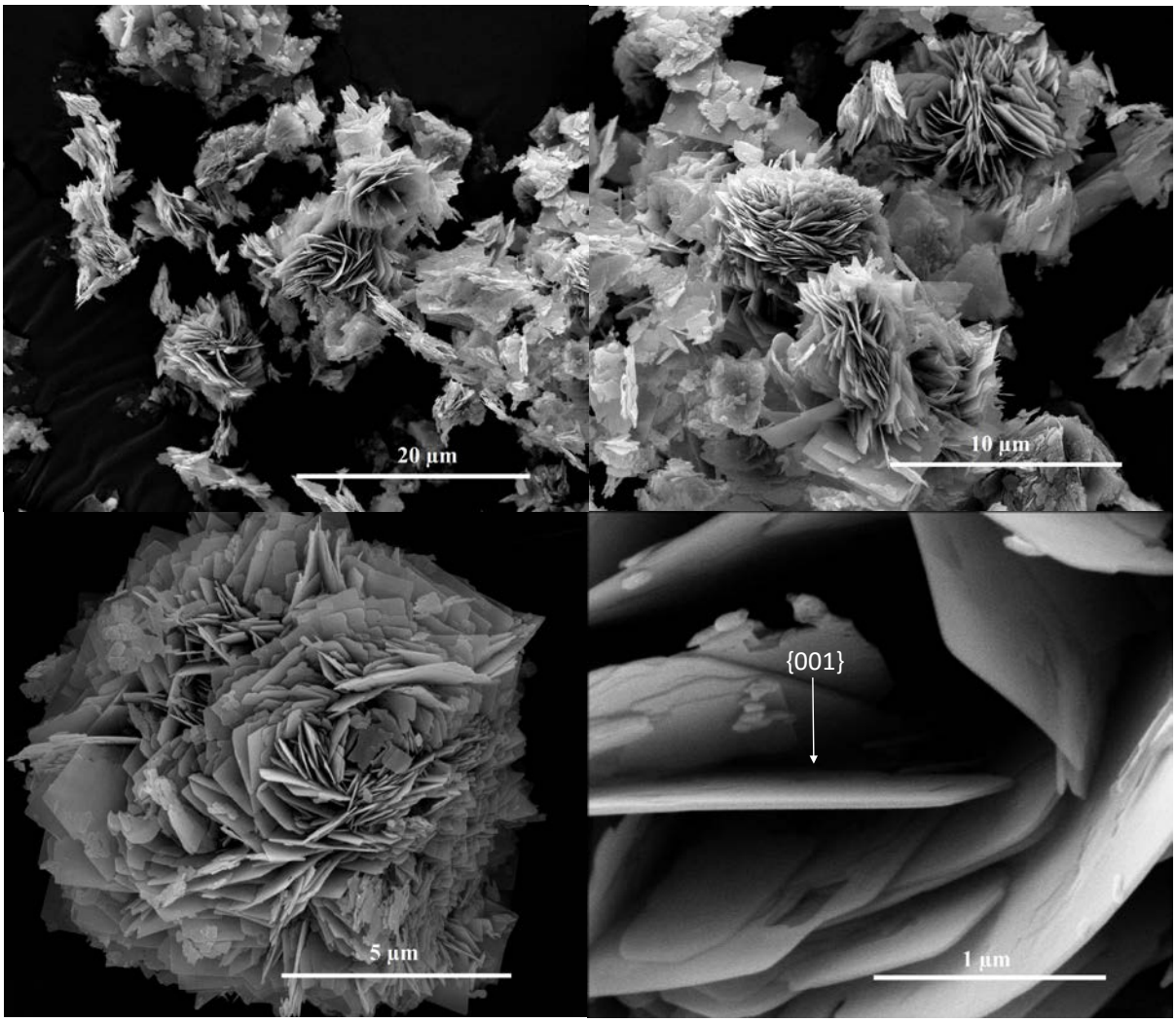

Figure S4. SEM images of the TiO_2 sheets obtained directly from TiF_4

1.3. Selected area electron diffraction

The results of performed selected area electron diffraction measurements for selected samples are presented in Figure S5, with a reflections for (101), (004) and (200) highlighted. Due to the particles aggregation obtained patterns exhibit polycrystalline character. The obtained results for SAED are consistent with XRD analysis.

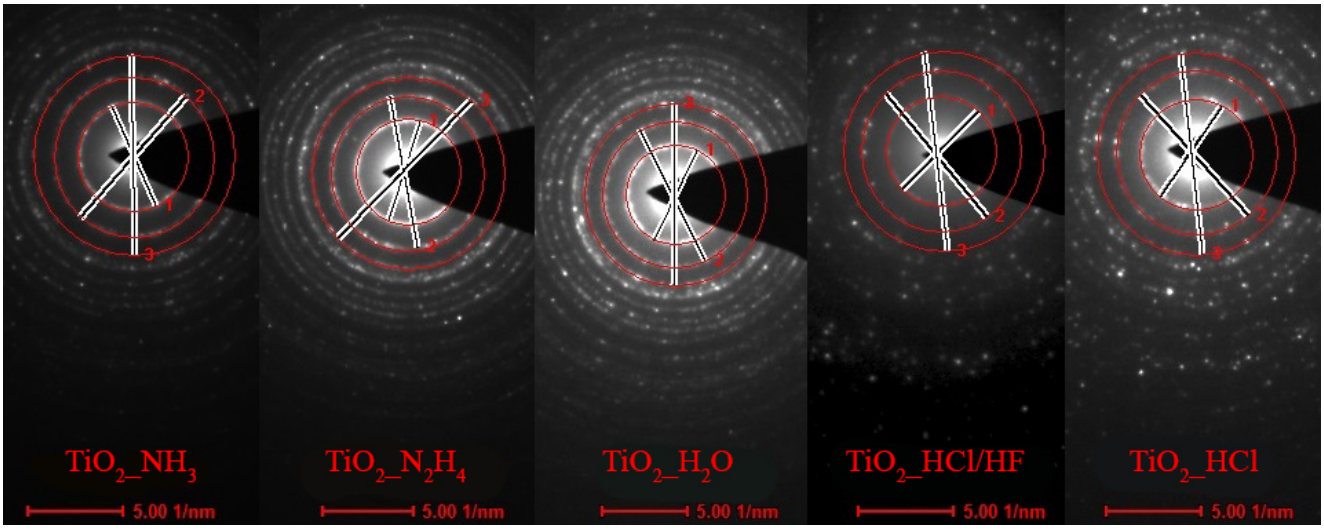

Figure S5. SAED patterns obtained for selected samples. Reflexes marked with 1, 2 and 3 correspond to the (101), (004) and (200) lattices respectively

The summary of the obtained results is presented in Table S3. The measurements were made using the transmission electron microscope (TEM) Tecnai 20F X-Twin, an electron source, cathode with field emission gun (FEG), EHT=200keV, camera for TEM Orius, Gatan Inc.

Table S3. Parameters of crystallographic structure determined from SAED diffraction patterns images.

Sample	distance, [1/nm]	d_{101}, [nm]	distance, [1/nm]	d_{004}, [nm]	distance, [1/nm]	d_{200}, [nm]
$TiOF_2$ + HCl	5.77	0.3466	8.41	0.2378	10.52	0.1901
$TiOF_2$ + HCl/HF	5.79	0.3454	8.46	0.2364	10.60	0.1887
TiOF2 + NH_3	5.80	0.3448	8.45	0.2367	10.60	0.1887
$TiOF_2$ + N_2H_4	5.78	0.3460	8.46	0.2364	10.60	0.1887
$TiOF_2$ + H_2O	5.78	0.3460	8.54	0.2342	10.60	0.1887
Mean value	5.78 ± 0.02	0.3458 ± 0.0012	8.46 ± 0.08	0.2363 ± 0.0023	10.58 ± 0.06	0.1890 ± 0.0011

1.4. Facet identification

Assuming the possible surface-presence of {001}, {101} and {100} facets, their identification has been based on the Wulff construct of the anatase crystal. By limiting only to the 3D structures, the combination of these 3 facets give a finite number of possible, unique crystal shapes, from which exposition of the specific facet can be deduced (as presented in Figure S6).

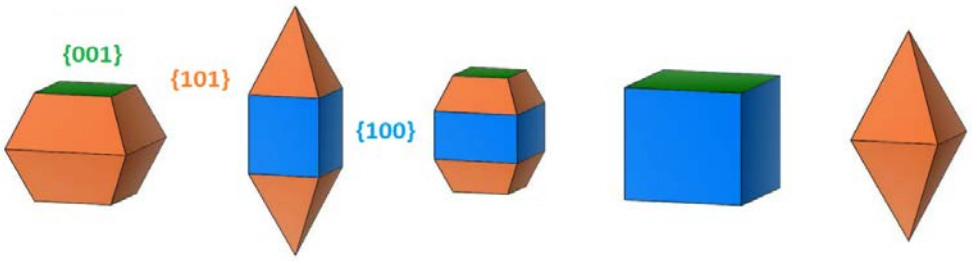

Figure S6. Possible 3D crystal shapes of anatase with exposition of {001} (green), {101} (orange) and {100} (blue) facets

Moreover, based on the Gibbs-Curie-Wulf theorem, the exposition of the specific facet should be proportional to its surface energy [44]. Therefore, the observed length of the facets of the same family should be approximately the same. Also, the symmetry of the crystal and surface (edge orientation) indicates which facets are observed. In this regard, the presence of the mentioned facets for each sample can be concluded, as presented in Figure S7.

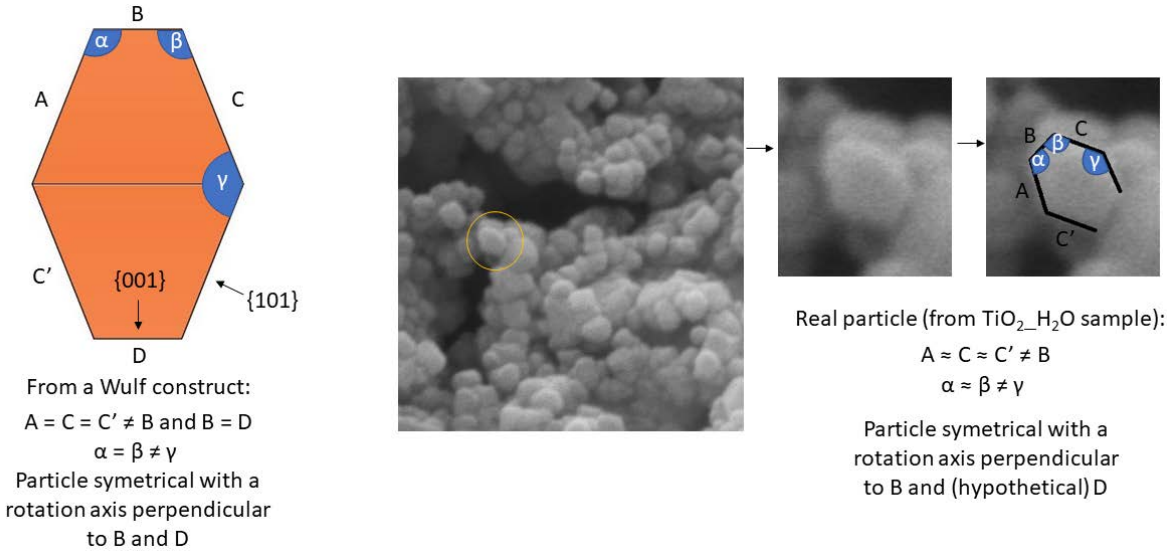

Figure S7. Example of identifying the crystal facets in SEM images, based on Wulff construction

To avoid the error during the observations (e.g. wrong identification of the {001} and {101} facets for decahedral particles, resulting from their similar edges lengths and some parts of the particle covered) the final results are presented as the statistical mean. The observations were made for a broader set of particles to achieve statistically consistent results ($n \geq 50$). It could also be noted that these shapes for anatase are well-established, and formation of {103} or {110} facets would result in different crystal shapes.

1.5. XPS studies

The survey scans of all samples (Figure S8) confirmed a low content of F^- ions and no additional elements except titanium, oxygen and carbon. Therefore, the influence of fluorine ions on shapes of TiO_2 nanostructures is negligible.

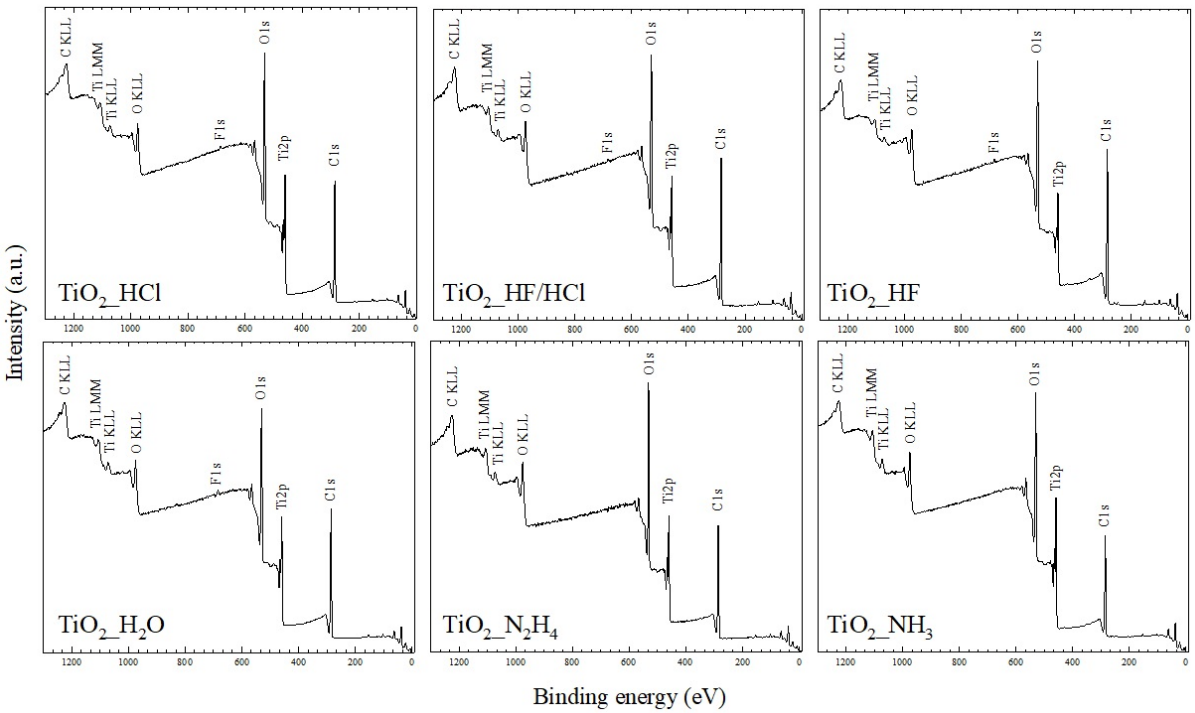

Figure S8. XPS survey scan of the TiO_2 nanostructures

1.6. Diffuse reflectance UV-Vis spectroscopy

The transformations of Kubelka-Munk function versus photon energy were presented in Figure S9. The calculated band gap energies for all of the obtained samples are close to a known value of anatase structure ~3.2 eV. The uncertainties of measurements come from the least squares approximation of linear jump of $(F_{KM} \cdot E_{ph})^{½}$ data and are included on the graphs.

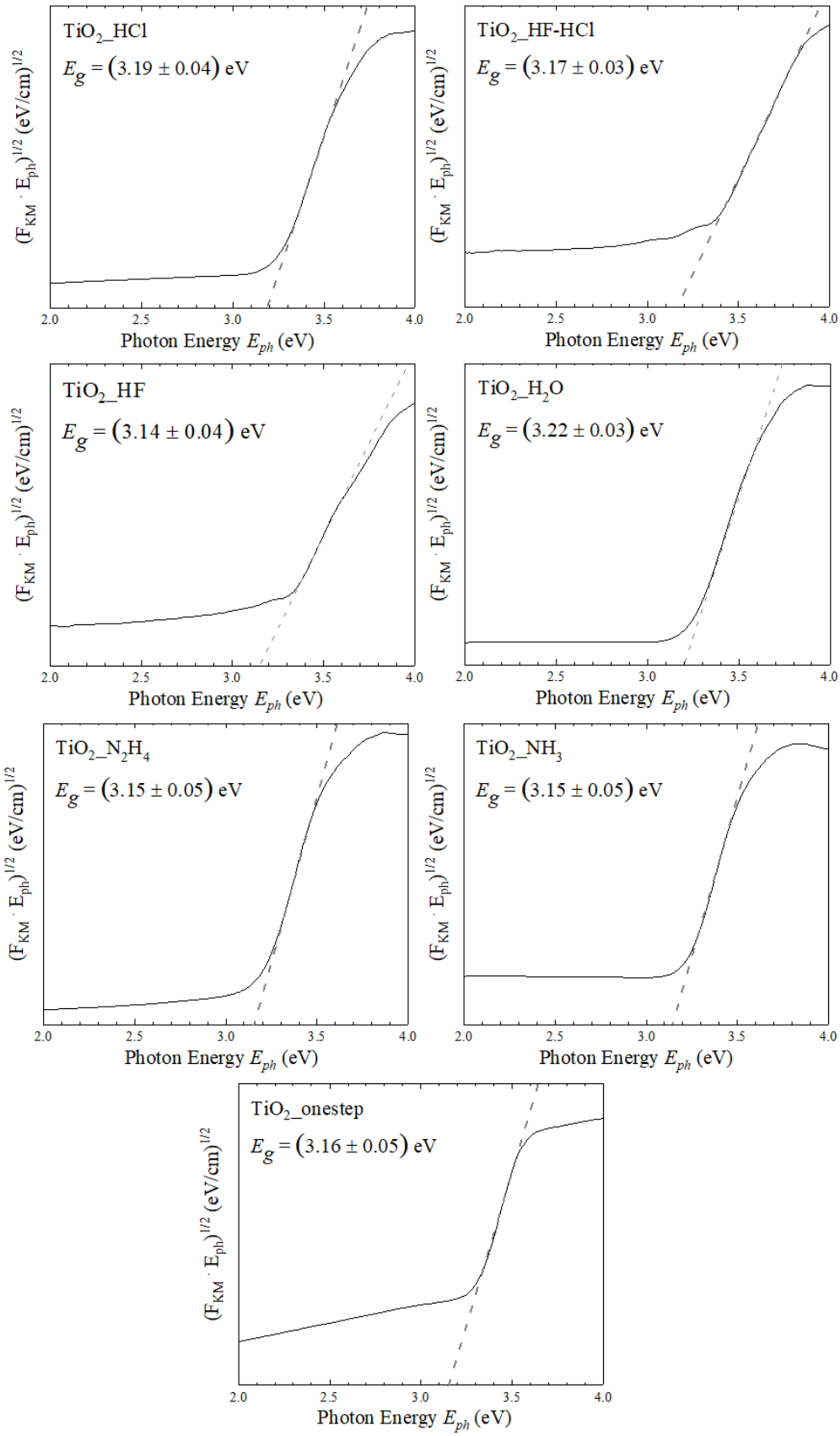

Figure S9. Tranformations of Kubelka-Munka functions versus photon energy for TiO_2 nanostructures

1.7. Photocatalytic activity comparison between direct and two-step processing of TiF_4

The photocatalytic activity of the obtained TiO_2 sheets (one step synthesis from TiF_4) was measured in the phenol degradation reaction, as described in the experimental section of the main text. Obtained results show phenol degradation of approximately 65% after 1 h of irradiation in the presence of prepared particles (see in Figure S10). This is significantly lower, than observed for samples prepared from $TiOF_2$ at the same process conditions. On the other hand, the phenol degradation was accompanied by the high rate of catechol formation, instead of hydroquinone, which fits well our observations of the (001) significance on its formation (see main text for other results and discussion). Since the (001) surface is known to be efficient at ·OH generation observed decrease in photocatalytic activity could be connected with the change of particles size and morphology, together with possible surface etching by introduced HF.

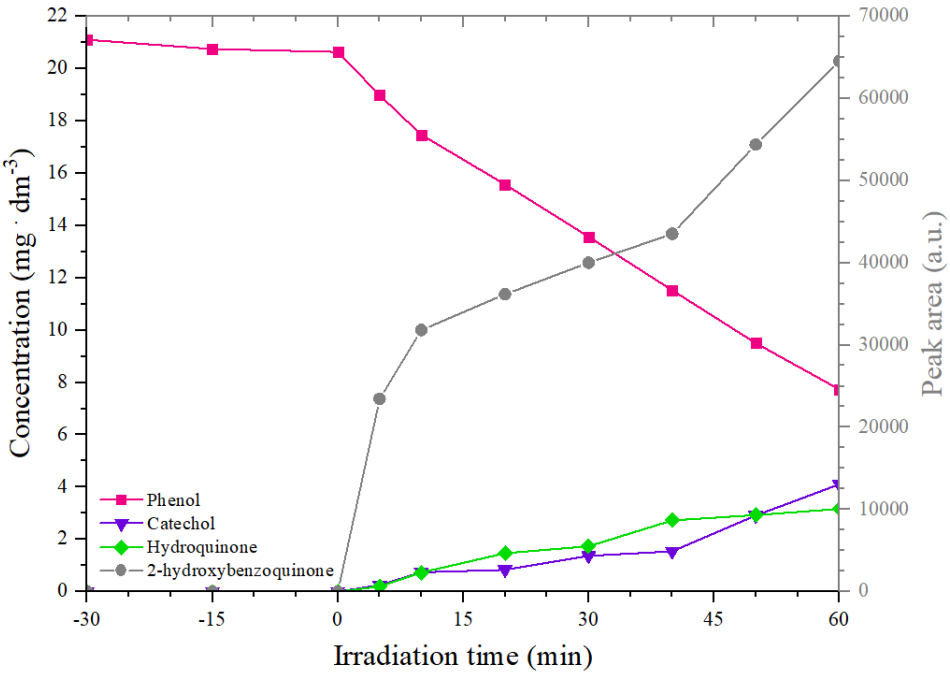

Figure S10. Phenol degradation in the presence of obtained TiO_2 sheets. The 2-HBQ signal (grey line) is given as observed peak area for 253 nm

1.8. Additional irradiations of benzoquinone and hydroquinone solutions

The additional irradiations of BQ and HQ solutions were performed for samples TiO_2_HF and TiO_2_N_2H_4 to identify the parent compound of additional derivative observed during the HPLC scan. These processes were performed an analogous way as for phenol, however, without any adsorption studies and only for 20 minutes. The BQ solution of approx. 35 mg·dm^{-3} and HQ of approx. 30 mg·dm^{-3} were used. The obtained results are shown in Figure S11. In both cases (that is, starting from HQ or BQ solution), sample TiO_2_HF has shown an increased intensity of 253 nm signal, which is in agreement with the results from phenol degradation. Moreover, an exceptionally high signal is observed when starting from the BQ solution, and some lower amount of considered derivative was observed already in the starting solution. Based on the observed absorption maxima and reported findings on BQ photolysis [69] observed compound is suggested to be 2-hydroxybenzoquinone (2-HBQ).

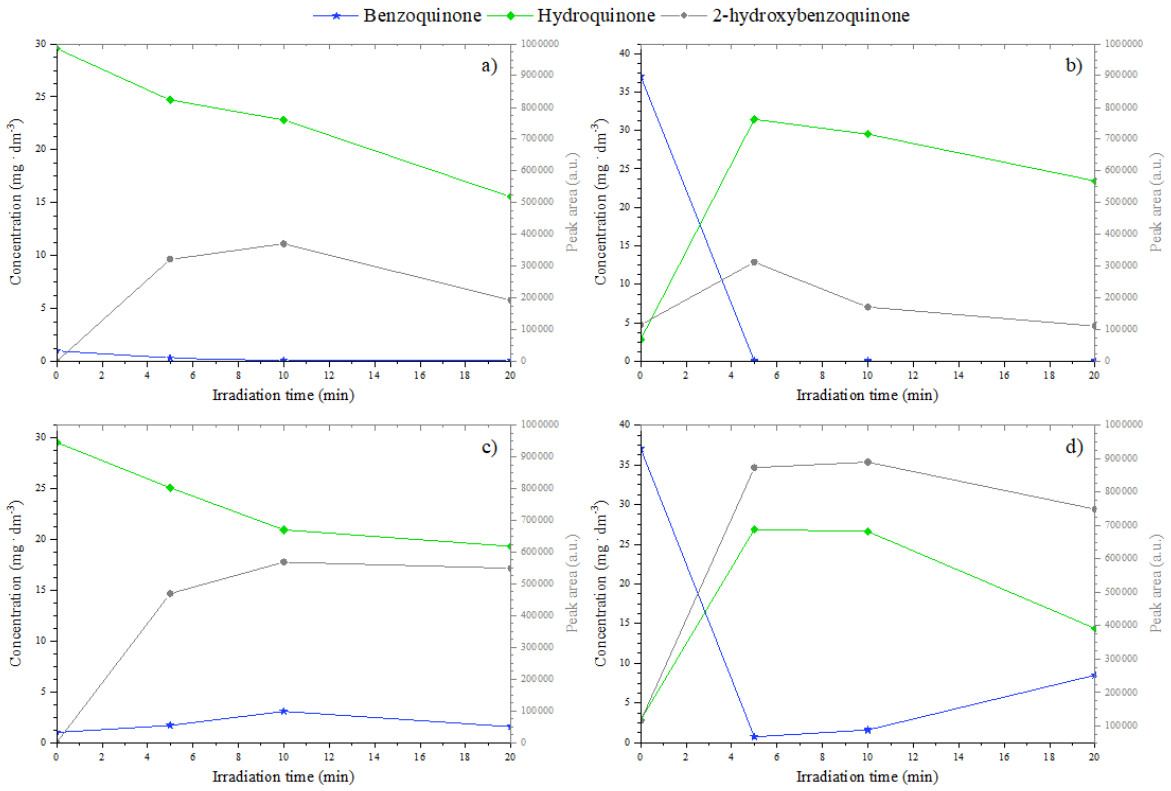

Figure S11. Hydroquinone and benzoquinone degradation in the presence of samples TiO_2_N_2H_4 (a,b) and TiO_2_HF (c, d). The 2-hydroxybenzoquinone signal is given as the peak are for 253 nm maximum

1.9. Minimum energy path calculations

The maximum energy images found during minimum energy path (MEP) calculations of ·OH and $\cdot O_2^-$ addition are shown in Figure S12. These images should be a close representation of a possible transition state (TS) complex formed during modelled reactions, however direct TS geometry was not optimized during this study. In a case of $\cdot O_2^-$ attack at *ortho* substitution the minimum energy image was also found, with a creation of hydrogen bond between the radical and -OH moiety, and this structure was also shown in detail (first structure in Figure S11-c). For all reactions, a final optimized structure is also shown. The energy results of MEP calculations are shown in the main text. Highlighted lengths are in Ångströms.

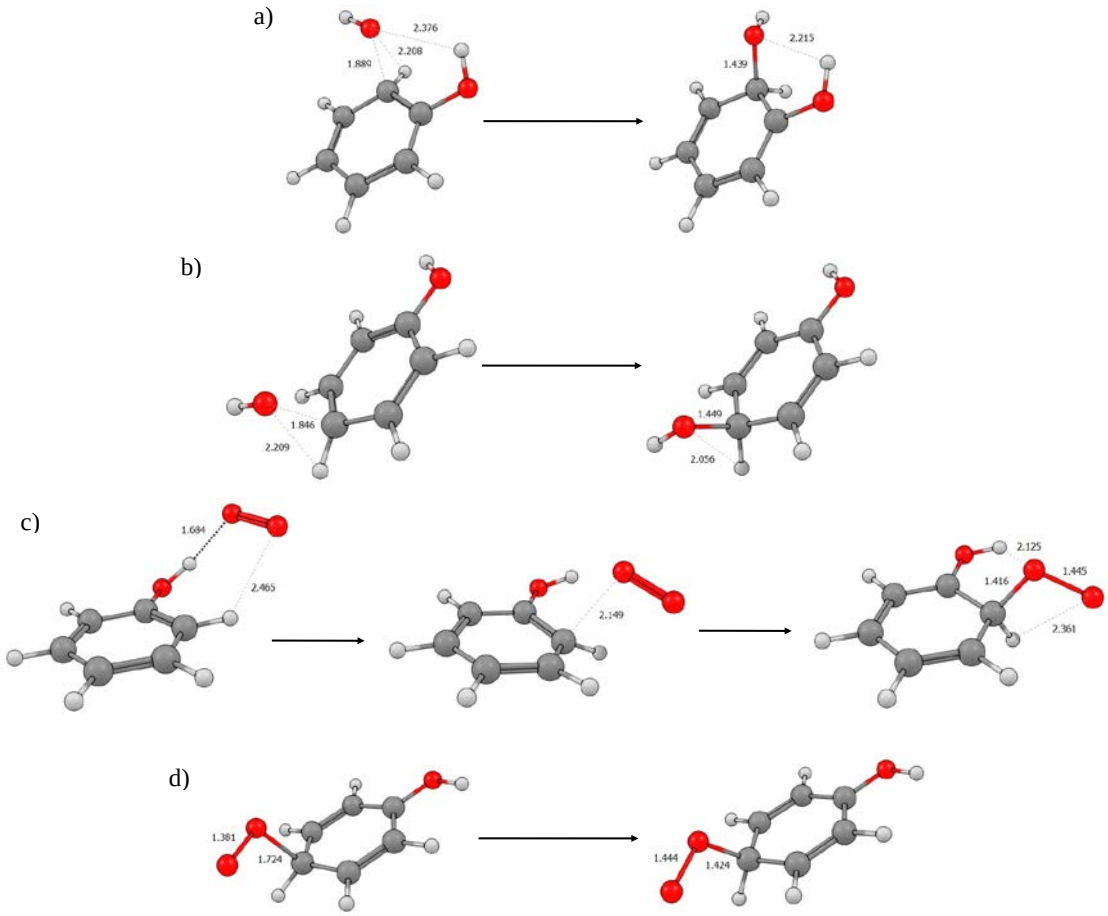

Figure S12. Specific structures found during MEP calculations of ·OH and $\cdot O_2^-$ substitution at specific position in phenolic ring: ·OH addition at *ortho* substitution (a); ·OH at *para* substitution (b); $\cdot O_2^-$ at *ortho* substitution (c) and $\cdot O_2^-$ at *para* substitution (d).